

– Supplemental Information –

**Observing the structural evolution in the photodissociation of
diiodomethane with femtosecond solution X-ray scattering**

Matthijs R. Panman,¹ Elisa Biasin,² Oskar Berntsson,¹ Markus Hermann,³ Stephan Niebling,¹
Ashley J. Hughes,¹ Joachim Kübel,¹ Kalina Atkovska,³ Emil Gustavsson,¹ Amke Nimrich,¹
Asmus O. Dohn,² Mads Laursen,² Diana B. Zederkof,² Alireza Honarfar,⁴ Kensuke Tono,⁵
Tetsuo Katayama,⁵ Shigeki Owada,⁶ Tim B. van Driel,⁷ Kasper Kjaer,² Martin M. Nielsen,² Jan
Davidsson,⁸ Jens Uhlig,⁴ Kristoffer Haldrup,² Jochen S. Hub,³ and Sebastian Westenhoff^{1, *}

¹*Department of Chemistry and Molecular Biology,
University of Gothenburg, Box 462, 40530 Gothenburg, Sweden*

²*Centre for Molecular Movies, Department of Physics,
Technical University of Denmark, DK-2800 Lyngby, Denmark[†]*

³*Georg-August-Universität Göttingen, Institute for Microbiology and Genetics,
Justus-von-Liebig-Weg 11, 37077 Göttingen, Germany*

⁴*Department of Chemical Physics, Lund University, Box 124, S-2210, Lund, Sweden*

⁵*Japan Synchrotron Radiation Research Institute,
1-1-1 Kouto, Sayo-cho, Sayo-gun, Hyogo 679-5198, Japan*

⁶*RIKEN SPring-8 Center, 1-1-1 Kouto,
Sayo-cho, Sayo-gun, Hyogo 679-5148, Japan*

⁷*LCLS, SLAC National Laboratory, Menlo Park, California 94025, USA*

⁸*Department of Chemistry, Ångström Laboratory,
Uppsala University, Box 523, SE75120 Uppsala, Sweden*

(Dated: October 15, 2020)

CONTENTS

Sample preparation and delivery	4
Time-resolved WAXS experiments	4
Run LN34 XPP LCLS	4
Run 2016A8037 BL3 EH2 SACLA	5
Transient absorption experiments	5
Excitation conditions	6
Isomer formation	6
Data analysis	7
Data reduction	7
Removal of the heat contribution to the difference-scattering data	8
Determination of the instrument response function	10
Computation of X-ray scattering of candidate structures	10
Scattering basics	10
Solute term	11
Solvent-solute cross-terms	11
Solvent-solvent terms	12
Contribution of the three components to the difference scattering	13
Scattering library for iodine-solvent contributions from Molecular Dynamics (MD) simulations	13
Potential energy surface calculation	14
Stability of geminate pair from MD simulations	15
Structural refinement against $\Delta S(q,t)$	16
Kinetic model of the revised reaction mechanism for the photo-dissociation of diiodomethane	17
Estimating the rotational diffusion correlation time of the $\text{CH}_2\text{I}^\bullet$ fragment	19
Estimating the translational and rotational kinetic energy of the $\text{CH}_2\text{I}^\bullet$ and I^\bullet fragments	20
Systematic evaluation of the considered chemical species in the modelling of the difference scattering	21

SAMPLE PREPARATION AND DELIVERY

250 μL diiodomethane (Sigma-Aldrich, ReagentPlus 99 %; Wako Pure Chemical Industries, Ltd., 1st Grade) was dissolved in 100 mL cyclohexane (Sigma-Aldrich, HPLC grade; Wako Pure Chemical Industries, Ltd., HPLC grade) resulting in a 50 mM solution. 0.89 g 4-bromo-4-(*N,N*-diethylamino)-azobenzene (heat dye, synthesized following Kjær *et al.* [1]) was dissolved in 100 mL cyclohexane resulting in a 17.1 mM solution. The amount of the samples were increased by a factor of 5 for the SACLA experiments. At the LCLS, the sample was supplied in the form of a round liquid jet with a diameter of 50 μm , which was available at the beamline. At SACLA, we used a home-built jet system (Fig. S1).

TIME-RESOLVED WAXS EXPERIMENTS

Time-resolved WAXS data were recorded at the X-ray pump-probe (XPP) instrument at the Linac Coherent Light Source (LCLS) XFEL facility (data in main text) [2] and experimental hutch EH2 of beam line BL3 at Spring-8 Angstrom Compact free electron LAser (SACLA) [3].

Run LN34 XPP LCLS

We used the standard configuration for run 14. Briefly, a focused monochromatic beam (3x3 μm , large-offset monochromator in diamond (111) configuration) of X-ray pulses, 9.5 keV, <50 fs FWHM, 10^{10} photons on average per pulse, 120 Hz repetition rate was spatially overlapped with a focused optical femtosecond laser pulse (130 \times 190 μm FWHM beam dimension, 266 nm, <60 fs FWHM, 8 μJ pulse energy) [4] in a near-collinear geometry in a cylindrical liquid jet (50 μm diameter). The sub-picosecond time-resolution between optical- and XFEL-pulses was achieved with a spectral-encoding technique (timing tool) [4, 5]. The overall time resolution was estimated to 90 fs by convolution of the Gaussian pulse shapes of the X-ray pulses, UV pulses and their velocity mismatch in the liquid jet (50 fs). The X-ray scattering patterns were recorded on the CSPAD detector placed \sim 6 cm after the sample, covering scattering vectors (q) up to 5 \AA^{-1} . A stable, round jet was achieved by running the sample at a flow rate of 2 mL min $^{-1}$ (or 17 ms $^{-1}$, HPLC pump) through a 50 μm (inner diameter) glass fiber. This flow rate results in a displacement of 14 cm of the sample between consecutive laser shots which is sufficient to provide a fresh sample for each probe pulse.

Run 2016A8037 BL3 EH2 SACLA

An unfocused pink beam of X-ray pulses (300 μm FWHM diameter, 11.980 ± 0.028 keV, 10 fs FWHM, 30 Hz repetition rate) was spatially overlapped with a focused optical femtosecond laser pulse (300 \times 400 μm FWHM beam dimension, 266 nm, <100 fs FWHM, 190 μJ pulse energy) in a near-collinear geometry in a liquid-sheet jet (100 μm thick). The actinic 266 nm light was generated by sum-frequency generation (SFG) of 800 nm and 400 nm light from an optical laser system consisting of a Legend Elite (Coherent) and an in-house-designed multi-pass amplifier (~ 15 mJ pulse energy, <40 fs FWHM pulse duration). The CPA system is synchronized to the XFEL operating frequency and is described elsewhere [6]. Sub-picosecond time-resolution (≈ 110 fs) between optical- and XFEL-pulses was achieved with a spatial encoding technique (timing tool) [7, 8]. The effective time resolution was estimated to be ~ 140 fs by convolution of the Gaussian pulse shapes of the X-ray pulses, UV pulses and their velocity mismatch in the liquid jet (100 fs).

The sample was placed at a distance of 62 mm from the detector (octal MPCCD) [9] which was vertically offset from the center by 80 mm. A beam stop was positioned between sample and a 50 μm thick Kapton window. These parameters afford us a usable momentum transfer range of $q = 0.53 \text{ \AA}^{-1}$ to 5.98 \AA^{-1} . The sample delivery was mounted such that the X-ray beam was normal to the plane of the liquid jet. The laser spot (450 μm FWHM) was overlapped with the X-ray beam (300 μm FWHM) at the sample position using two remote-controlled microscope cameras. The laser and X-ray beams propagated horizontally with respect to the laser table in a near co-linear geometry (5–10°). The light intersected the sample at a 300 μm offset below the nozzle outlet. At this position, the liquid-sheet thickness is the most stable. The chamber was kept under an He atmosphere.

TRANSIENT ABSORPTION EXPERIMENTS

The beam diameter of the pump was 226 μm FWHM (determined with a knife-edge measurement) at the focal point. The pump power was controlled with a continuously-variable neutral-density filter wheel, and measured with a thermophile power meter. Pump and probe beams were spatially overlapped in a near co-linear geometry in a flat-sheet liquid jet (50 μm thickness) of a solution of 50 mM CH_2I_2 in cyclohexane. All recorded transient spectra were corrected for chirp of the white-light probe pulses. The pump-pulse duration was 80 fs. Figure S3 shows the difference

absorption of the 266 nm excitation of diiodomethane in cyclohexane.

Excitation conditions

Fig. S2 displays the fluence dependence of the differential absorption and scattering of pure cyclohexane and CH₂I₂ in cyclohexane. The transient absorption data show that the excitation fluence for the time-resolved WAXS data shown in the main text (30 mJ cm⁻²) is in the linear regime (Fig. S2 panels (b) and (c)). A small two-photon component of direct absorption into the solvent is also observed (Fig. S2 panel (a), (c), (d)) which manifests as extra heat in the scattering data (Fig. S2 panel (d)). The solvent-heating scattering contribution is effectively subtracted from the data prior to the structural fitting and included in the structural fitting.

Isomer formation

The interpretation of the transient-absorption signal (ΔA) has been discussed at length [10–12]. Briefly, the vibrational excitation of the photoproducts is a prominent feature in the signal for delays up to ~ 20 ps after excitation. The dissociation of the CH₂I₂ molecule results in a CH₂I[•] fragment with a high degree of internal excitation (~ 240 kJ mol⁻¹ [12]). The nascent H₂CI–I isomers are therefore highly vibrationally excited which manifests as a broad positive band with $\lambda_{\text{max}} = 400$ nm, at 10 ps to 50 ps after excitation (see Fig. S4((a))). The subsequent vibrational cooling causes a blue-shift and narrowing of this band to a final band position at 390 nm, which is the characteristic absorption of the H₂CI–I transient isomer. The formation of the isomer was estimated to occur with a life time of $t < 1$ ps (due to the presence of non-zero amplitude at 1 ps) and ~ 5.5 ps (obtained by spectral integration of the vibrationally-broadened band [12]). These findings are supported by transient Raman performed on the isomer band at 400 ns [13].

The time dependence of the isomer band is complex (Fig. S4(b)). After the initial photoexcitation ($t > 1$ ps) the increase of the difference absorption at 390 nm occurs with multiple time constants. We observe the ~ 15 ps growth reported in literature, which corresponds to the lifetime ($\tau_1 = 8$ ps) extracted from the amplitudes of the species of the TRWAXS structural fit (see main text).

The analysis of the kinetics approaching 1 ns is made difficult, because multiple species overlap in the spectra region around 400 nm [14–16]. It is advantageous to use TRWAXS for discrimina-

tion of the photoisomer against other species, because of the characteristic short I···I bond length.

DATA ANALYSIS

The data analysis was implemented in Matlab[®] software (The MathWorks, Inc.) and Python 3.6 using the packages Numerical Python, Scientific Python, Matplotlib [17]. The least-squares fits were performed using the Lmfit package [18] and implemented in Matlab[®]. For all the fits, we used the Levenberg-Marquardt algorithm to minimize χ^2 , defined as:

$$\chi^2 = \sum_{j=1}^n \frac{(y_j^{\text{obs.}} - y_j^{\text{calc.}})^2}{\sigma_j^2}, \quad (\text{S1})$$

where $y_j^{\text{obs.}}$ is an observed quantity in the j^{th} bin (this can be a delay point, q point, amplitude, etc.), $y_j^{\text{calc.}}$ the corresponding calculated quantity, and σ_j the measurement error in the observed quantity. All the reported uncertainties in the parameter values are standard errors obtained from the variance-covariance matrix after the final iteration of the least-squares fit. $\sigma_j = 1$ in the case of the structural refinements shown in Fig. 1(a), Fig. S13, and Fig. S14. For the kinetic fits in Fig. 2(a) and (b) σ_j was taken from the standard error determined by the structural refinement.

Data reduction

Each scattering pattern was corrected for the background, solid angle coverage, X-ray polarization and common mode fluctuations [19, 20]. The sample-detector distance was calibrated by comparing the azimuthally integrated total scattering signal to a reference measurement of neat cyclohexane [21]. This reference measurement was also used to scale (in the q range 0.7 \AA^{-1} to 4 \AA^{-1}) the measured signal to the scattering signal arising from a liquid unit cell [19], yielding the measured signal in electron units per solute molecule (e.u. molec.^{-1}). For every seventh shot scattering patterns were recorded without optical excitation (laser-off scattering patterns). Difference-scattering patterns were constructed by subtracting the average of the ten nearest laser-off scattering patterns. For time delays < 2 ps, each difference scattering pattern was time stamped with 10 fs (FWHM) resolution using the timing tool [5]. The difference scattering patterns were then time sorted and averaged into time bins of 40 fs width, each containing ~ 6400 curves. For time delays > 2 ps, the signal was measured at selected time points up to 1 μs and ~ 4000 shots

were averaged per time point. The averaged difference scattering patterns were (1) azimuthally integrated and (2) azimuthally integrated in 15 slices, from which the isotropic and anisotropic difference scattering signals were extracted as described in detail in Biasin *et al.* [22].

At SACLA, the X-ray scattering patterns were collected on the MPCCD detector, that was offset from the center so that q range was covered up to $\approx 6 \text{ \AA}^{-1}$. A similar procedure to that described above was applied for the correction and reduction of the scattering patterns to one-dimensional curves. For early time scale (<2 ps) ~ 1000 shots were averaged in ~ 70 fs wide time bins. At later time scale (up to 300 ps), ~ 300 shots were averaged for each time point.

Removal of the heat contribution to the difference-scattering data

A significant part of the photon energy absorbed by the sample is released as heat to the solvent, creating a significant contribution to the acquired WAXS signal. In the case of cyclohexane, the difference signal is quite different from that of the solute, having very distinctive, sharp peaks between $q = 0.5 \text{ \AA}^{-1}$ to 1.75 \AA^{-1} (Fig. S5) [1] and it can therefore be subtracted from the data. To do so, we measured the heating signal of the cyclohexane by recording the time-resolved WAXS signal of 4-bromo-4-(*N,N*-diethylamino)-azobenzene (heat dye) in cyclohexane (Fig. S5(a)) using the same setup as for the experiments on diiodomethane. We applied a Singular Value Decomposition (SVD) to the dye data, which yielded two significant projection vectors $U^{\Delta S^H}(q, n)$ (Fig. S6 and S7(a)). Minimization of the residual between $U^{\Delta S^H}$ and experimental $\Delta S(q)$ would result in inaccurate amplitudes of the heat components $A(t, n)$. Therefore, we developed a more accurate method to subtract the heat (see Fig. S7(a) for a schematic overview of the procedure). First we filtered the heat SVD projection vectors $U^{\Delta S^H}$ with a Fourier filter, computed the 2nd derivative, and filtered the heat data again (see Fig. S7(b)). We also filtered the $\Delta S(q)$ of the diiodomethane and computed its 2nd derivative. The $A(t, n)$ of the first two heat components were then determined by a least-squares fit in 2nd derivative (Fig. S7(c)). Subsequently, the two most significant heat components $U^{\Delta S^H}$ were scaled with $A(t, n)$ and subtracted from the difference-scattering data to yield the heat-corrected difference scattering $\Delta S^C(q, t) = \Delta S(q, t) - [U^{\Delta S^H}(n = 1) \cdot A(t, n = 1) + U^{\Delta S^H}(n = 2) \cdot A(t, n = 2)]$ (see Fig. S7(d)). Using the 2nd derivative is rationalized, because we found that the 2nd derivative of the structural signal $d(\Delta S(q))^2/d^2q$ resembles that of the heat components $d(U^{\Delta S^H})^2/d^2q$ (left panel of Fig. S7(c)) much more closely than the original signals $\Delta S(q)$ and $U^{\Delta S^H}$ (left panel of Fig. S7D). This is because the 2nd deriva-

tive amplifies the high-frequency components of a signal (noise and heat) and reduces the low-frequency components (the structural signal). Noise is also amplified by taking the 2nd derivative, which necessitates the filtering processes. As a general note, care should be taken not to filter the curves too heavily as this would flatten the curve in question and result in an overestimation of the amplitudes $A(t, n)$. Comparison between the raw- and heat-subtracted data (respectively Fig. S5(c) and S13 for the run LN34; respectively S5(b) and S14 for run 2016A8037) reveals that the procedure removes the heat signals. We note that due to the high-frequency nature of the heat signal, an imperfect subtraction would likely not bias the structural refinement. Nonetheless, we included the solvent-heat response in the structural refinement to compensate for a possible imperfect subtraction.

We performed a kinetic analysis on the extracted heat response. We reconstructed the heat difference scattering from the three SVD components ($U^{\Delta S^H}(q, n)$) and their amplitudes ($A(t, n)$) obtained from the heat subtraction method (Fig. S7). Subsequently, we performed a least-squares fit of the reconstructed heat signal (Fig. S8(a)) with a triple-exponential function:

$$f(t) = \left(\sum_{i=1}^n A_n \cdot (1 - \exp(-k_n \cdot (t - t_0))) \right) \cdot \left(\frac{\delta S}{\delta T} \right)_\rho \quad (\text{S2})$$

with $(\delta S / \delta T)_\rho$ as heating difference scattering signal of cyclohexane at constant density, taken from Ref. [1]. The lifetimes obtained from the fit are $\tau_0 = 0.61 \pm 0.04$ ps, $\tau_1 = 18 \pm 2$ ps, and $\tau_2 = 700 \pm 200$ ps (errors obtained from the fitting procedure) see Fig. S8(b). The first lifetime corresponds well with an ultrafast vibrational relaxation of the bath modes, thus reflecting the time that it takes for the pressure to build up [1]. The the second refined lifetime (18 ps) is longer than the first formation time of the photoisomer (8 ps from structural fit), but corresponds well to the vibrational cooling of the $\text{CH}_2\text{I}^\bullet$ fragment (20 ps) (reference [12], and Fig. S3 and Fig. S4(a)). We believe that both processes contribute to the increase in heat. Even though the third lifetime is apparently faster than the second isomer formation lifetime, (0.7 ns versus 2.8 ns), we believe that the times agree within the accuracy of the measurement, because we collected only very few data points in the 0.5 ns to 2.8 ns time window.

Determination of the instrument response function

The instrument response function (IRF) was determined by a least-squares fit of the following model to the difference scattering signal integrated over a q -range spanning 2 \AA^{-1} to 4.5 \AA^{-1} :

$$f(t) = 0.5 \cdot \sum_{i=1}^n \left(A_n \cdot \exp \left(\frac{(\sigma^2 - 2 \cdot (t - t_0) \cdot \tau_n)}{(2 \cdot \tau_n^2)} \right) \cdot \operatorname{erfc} \left(\frac{(\sigma^2 - (t - t_0) \cdot \tau_n)}{(\sqrt{2} \cdot \sigma \cdot \tau_n)} \right) \right) + O, \quad (\text{S3})$$

with the relative timing between the center of the pulse and the nominal delays t_0 , the pulse duration σ , the amplitude of the n^{th} component A_n , the lifetime of the n^{th} component τ_n , and the offset O . We found two components were necessary to minimally fit the integrated ΔS signal (see Fig. S9). We found $\sigma = 80 \pm 10$ fs.

Computation of X-ray scattering of candidate structures

Scattering basics

The structure factor ($A(\mathbf{q})$) of a sample is given by:

$$A(\mathbf{q}) = \int \rho_e(\mathbf{r}) e^{-i\mathbf{q} \cdot \mathbf{r}} d\mathbf{r}, \quad (\text{S4})$$

where $\rho_e(\mathbf{r})$ is the electron density in the sample, \mathbf{q} is the scattering vector with the modulus q ($q = 4\pi \sin(\theta)/\lambda$ where 2θ is the scattering angle and λ the X-ray wavelength), and \mathbf{r} is the position vector. Assuming spherical averaging, the scattering intensity of the sample is:

$$S(q) = \langle A(\mathbf{q}) A^*(\mathbf{q}) \rangle_{\Omega} = \int \rho(r) \operatorname{sinc}(qr) dr, \quad (\text{S5})$$

where $\langle \cdot \rangle_{\Omega}$ denotes the orientational average. $\rho(r)$ is the pair distance distribution function of the electron density of the sample and therefore contains information about all distances in the sample. The total scattering is separated into a solvent (S), solute (I), and a cross-scattering term:

$$S(q) = S_{II}(q) + S_{SI}(q) + S_{SS}(q). \quad (\text{S6})$$

In real space this corresponds to separating ρ into three parts: ρ_{II} , ρ_{SS} , and ρ_{SI} . The scattering then becomes:

$$S(q) = \int \rho_{II}(r) \text{sinc}(qr) dr + 2 \int \rho_{SI}(r) \text{sinc}(qr) dr + \int \rho_{SS}(r) \text{sinc}(qr) dr . \quad (\text{S7})$$

Solute term

We express S_{II} in terms of the Debye equation (also known as the Independent Atom Model, or IAM):

$$S_{II}(q) = \int \rho_{II}(r) \text{sinc}(qr) dr = \sum_i F_I^2(q) + F_I^2(q) \sum_{i,j,j \neq i} \text{sinc}(qd_{ij}) , \quad (\text{S8})$$

with F denotes the atomic form factors and d_{ij} as the distance between two atoms. In our system, the sums run over the two iodine atoms. When computing the difference scattering, the first term F_I^2 (the self-scattering term) cancels.

Solvent-solute cross-terms

Following Ref. [23, 24], the scattering of the cross term S_{IS} is defined as:

$$S_{IS}(q) = 2 \int \rho_{SI}(r) \text{sinc}(qr) dr = 2 \sum_{s=\{H,C\}} F_I F_s \rho_{s,0} N_I 4\pi \int (\gamma_s(r) - 1) r^2 \text{sinc}(qr) dr . \quad (\text{S9})$$

s denotes the atom types in the solvent (H and C in our case, not to be confused with capital S, which denotes ‘solvent’). $\rho_{s,0}$ is the number density of the solvent atom type s in the bulk, at a long distance from the solute. $\gamma_s(r)$ is the pair distance correlation function between the iodine atoms and solvent atoms s , which was obtained from molecular dynamics simulations (see section for iodine-solvent contributions from Molecular Dynamics (MD) simulations). Here, $\gamma_s(r)$ was normalized by the number of solute atoms and by the number density of solvent atoms, such that $\gamma_s(r)$ approaches unity at large r . Truncation errors introduced by the necessarily limited simulation-box size are mitigated using an exponential damping factor ($\exp(-(r/\mu - 1)^2)$) for $r \geq \mu$ before substituting in Eq. S9. The -1 in Eq. S9 is necessary since the relative electron densities are in respect to the bulk density of the solvent. The factor 2 comes from equation S7 (cross terms arising in each direction once) and N_I is the number of solute atoms in the system ($N_I = 2$ for this case).

Solvent-solvent terms

The shape of the solvent pocket is expected to change as the solute molecules evolve structurally. Therefore, we included a solvent-solvent contribution into the difference scattering. Analogous to the solute-solvent cross-term, one could derive the solvent-solvent term by extracting the pair-distance correlation functions ($\gamma_{ss}(r)$) from molecular dynamics simulations. However, it is difficult to reliably extract this quantity from MD simulations due to the limited size of the box and instabilities of the densities at large distances.

Therefore, we adopted a different strategy and approximated the solvent-solvent term as scattering from dummy atoms, which were assumed to be placed at the same positions as the solute atoms. This strategy is widely used for computation of protein X-ray scattering. The approach is attractive, because the scattering of the dummy atoms can then be computed using the Debye equation. For protein scattering, the electron density of the dummy atoms is often modeled as Gaussian spheres, which are then scaled by the volume of displaced solvent (or displaced volume, DV) and the solvent electron density [25]. Here we obtained the electron density of the dummy atoms from the atom densities of the solvent surrounding the iodine atoms, as given by radial distribution functions $\gamma_s(r)$ ($s = \text{C, H}$) determined by molecular dynamics simulations. The use of this refined description of the solute-solvent correlation is expected to increase the accuracy of the computation, because it is based on a physically realistic structure of the solvent around the solute.

The electron density of a dummy atom, which has the same position as the iodine atoms, is then given via $(\gamma_s(r) - 1)$, convolved with the electron density $\rho_s^{\text{el}}(\mathbf{r})$ around the solvent atoms,

$$p_{DV}(\mathbf{r}) = \sum_{s=\{\text{H,C}\}} \rho_{s,0} \int d\mathbf{r}' (\gamma(|\mathbf{r}'|) - 1) \rho_s^{\text{el}}(\mathbf{r} - \mathbf{r}'). \quad (\text{S10})$$

The -1 within the integral accounts for the fact that the hole represents a difference electron density relative to the bulk solvent. At small r , $p_{DV}(\mathbf{r})$ is negative, which is consistent with a cavity; at large distance r from the iodine, where $\gamma(r)$ approaches unity, $p_{DV}(\mathbf{r})$ approaches zero. The form factor of the dummy atom is the Fourier transform of $p_{DV}(\mathbf{r})$. Using the convolution theorem of Fourier transforms, and carrying out an orientational average, we obtain

$$F_{DV}(q) = a_{DV} 4\pi \sum_{s=\{\text{H,C}\}} F_s(q) \rho_{s,0} \int (\gamma_s(r) - 1) r^2 \text{sinc}(qr) dr, \quad (\text{S11})$$

where a_{DV} is a scale factor which accounts for the error in molecular volumes obtained from MD simulations. The parameter can be obtained when fitting Eq. S11 to data. $F_s(q)$ is the form factor of solvent atom s , that is the orientationally averaged Fourier transform of ρ_s^{el} . Approximating the three-dimensional form factor $F_{DV}(\mathbf{q})$ with the orientational average $F_{DV}(q)$ is valid in our case because the solvent-solvent term gives a relatively small contribution to the overall scattering intensity.

In practice, F_{DV} was computed from an average of the two solute molecules present in the MD simulations (see section for iodine-solvent contributions from Molecular Dynamics (MD) simulations). The solvent-solvent term is then computed using the Debye equation with respect to the dummy atoms

$$S_{SS} = \sum_i F_{DV,i}^2 + 2 \sum_{i,j>i} F_{DV,i} F_{DV,j} \text{sinc}(qd_{ij}). \quad (\text{S12})$$

Note that F_{DV} depends on the positions of the solute atoms, the self-scattering (first) term can therefore not be neglected when computing difference scattering.

Contribution of the three components to the difference scattering

The computed scattering for different I...I distances corresponding to the optimal fits of **GP**₁, **GP**₂, **PI**, and the solvent-separated pair (geminate pair with an average $R_{\text{I...I}} = 4.35 \text{ \AA}$, geminate pair with an average $R_{\text{I...I}} = 5.40 \text{ \AA}$, the photoisomer $R_{\text{I...I}} = 3.13 \text{ \AA}$, and the solvent-separated pair with a fixed $R_{\text{I...I}} = 100 \text{ \AA}$, respectively) are shown in Fig. S10. The solute contributes to differences in the entire q -range, the solute-solvent term mainly contributes to the difference scattering for $q < 2 \text{ \AA}^{-1}$ and the solvent-solvent (displaced volume) term contributes at q -values below 1.3 \AA^{-1} . The absolute magnitude of the contributions in descending order are: the solute term; the solvent-solute term; and finally the displaced volume term.

Scattering library for iodine-solvent contributions from Molecular Dynamics (MD) simulations

To allow the computationally efficient fitting of structures of **I**[•] and **CH**₂**I**[•] against TR-WAXS data, we build a library of calculated scattering intensities using MD simulations. Scattering contributions due to iodine-carbon and iodine-hydrogen correlations were computed, $S_{Is}(q, R_{\text{I...I}})$, where s denotes C or H, respectively. $S_{Is}(q, R_{\text{I...I}})$ were computed from two iodine atoms at distance $R_{\text{I...I}}$ in cyclohexane. The contribution of the CH₂ group of **CH**₂**I**[•] was neglected, justified

by the fact that the CH₂ group provides a much smaller contrast with respect to the cyclohexane solvent as compared to the two iodine atoms. Furthermore, this approximation provides intensities with only one parameter ($R_{I...I}$), thereby avoiding over-fitting. $S_{IS}(q, R_{I...I})$ was computed for distances $R_{I...I}$ between 0.04 and 2.5 nm in steps of 0.02 nm (124 distances total). Fig. S17 shows the 124 curves used in the fitting procedure.

The MD simulations were set up as follows. Two iodine atoms with distance $R_{I...I}$ were placed into a cuboid simulation box, keeping a distance of 2 nm between iodine and the box boundary. The box was solvated by cyclohexane using a pre-equilibrated cyclohexane simulation box. Iodine atoms were modeled as Lennard-Jones (LJ) spheres, using LJ parameters $\sigma = 0.38$ nm and $\epsilon = 2.092$ kJ mol nm⁻² taken from the General Amber Force Field (GAFF) [26]. Parameters for cyclohexane were taken from the GAFF topology deposited at virtualchemistry.org [27]. The energy of each system was minimized, and each system was simulated for 5 ns. During the simulation, the positions of the iodine atoms were frozen, such that the pre-selected distance $R_{I...I}$ was maintained.

The simulations were carried out with the GROMACS simulation software, version 4.68 [28]. The temperature was controlled at 293.15 K using a stochastic dynamics integration scheme [29] ($\tau = 0.5$ ps), and the pressure was kept at 1 bar using the weak coupling scheme [30] ($\tau = 0.5$ ps). Bond lengths of the solvent were constrained using LINCS [31], allowing a time step of 2 fs. Dispersive interactions and short-range repulsion were described by a Lennard-Jones potential with a cut-off at 1.2 nm. Electrostatic interactions were truncated with a plain cutoff at 1.2 nm, justified by the fact that electrostatics hardly contribute to the potential energy energy in this apolar system.

For each $R_{I...I}$, after removing the first 40 ps for equilibration, the radial distributions functions between the iodine and carbon $\gamma_C(r, R_{I...I})$ and between iodine and hydrogen $\gamma_H(r, R_{I...I})$ was computed and used as outlined above. For iodine-iodine distances $R_{I...I}$ between the $R_{I...I}$ -values contained in the library, $S_{IS}(q, R_{I...I})$ was linearly interpolated.

Potential energy surface calculation

The potential energy surface of the I[•] radical around the CH₂I[•] radical was derived using high-level quantum-chemical calculations. We carried out multi-reference configuration interaction calculations with a complete active-space reference wave function with 14 electrons in 8 orbitals

(CASSCF(14,8)-MRCI). Since the exact nature of the active and inactive species involved in the radical pair is uncertain, a triplet electronic configuration was chosen in the modelling to prevent isomer formation. The calculations were conducted with ORCA [32, 33], version 4.0.1.2, with the def2-SVP [34] basis set and the relevant effective core potentials (ECPs) [35]. The $\text{CH}_2\text{I}^\bullet$ fragment was positioned such that the iodine was at the origin, while the plane defined by the four atoms was in the x - y plane. Then, the I^\bullet radical was moved in the x - y plane in steps of 0.2 Å, and the energy was computed. To obtain the potential energy relative to the dissociated state, we calculated the energy relative to the upper left corner in Fig. 2(c) and Fig. S11.

Stability of geminate pair from MD simulations

To rationalize the stability of the geminate pair against dissociation, we carried out classical molecular dynamics (MD) simulations of the $\text{CH}_2\text{I}^\bullet + \text{I}^\bullet$ pair in cyclohexane. The dispersive interactions and short-range repulsion between the two iodine atoms was described by a Buckingham potential fitted against a quantum-chemical potential energy scan at the CASSCF(14,8)-MRCI level of theory, as described above. Here, the position of the I^\bullet was scanned along a line such that the C-I and the I-I lines formed an angle of 135° (Fig. S11(c), black dots). The optimized Buckingham potential was $V_{\text{II}}(r) = A \cdot \exp(-Br) - C/r^6$, with $A = 123\,670 \text{ kJ mol}^{-1}$, $B = 22.076 \text{ nm}^{-1}$, and $C = 0.1073 \text{ kJ mol}^{-1} \text{ nm}^6$ (Fig. S11(c), red line). The bond lengths and angles of $\text{CH}_2\text{I}^\bullet$ were taken from a structure that was optimized at the BP86/def2-SVP level of theory, which led to the following parameters: H-C bond, 0.1097 nm; C-I bond, 0.206 nm; H-C-I angle, 117.25° , H-C-I angle, 125.51° . All other parameters were taken from the General Amber Force Field (GAFF) [26].

The $\text{CH}_2\text{I}^\bullet + \text{I}^\bullet$ pair was placed in a cubic simulation box and solvated with 178 cyclohexane molecules (inset Fig. S11(d)). After an energy minimisation, the system was simulated 30 times for 50 ns using the GROMACS simulation software, version 2016.3 [36]. Each simulation was started with newly and randomly assigned initial velocities, leading to 30 independent trajectories. The Buckingham potential was implemented using the GROMACS functionality for tabulated potentials. Lennard-Jones, the Buckingham, and Coulomb potentials were truncated at 1.4 nm. The pressure was controlled at 1 bar using the weak coupling scheme ($\tau = 5 \text{ ps}$) [37]. The temperature was controlled at 293.15 K using a stochastic dynamics integrator with a large time constant ($\tau = 2 \text{ ps}$), such that the influence of the friction term on the dissociation rate of the geminate pair was negligible. Other parameters were taken as described above.

After removing the first 5 ns of equilibration time from each trajectory, the time that the geminate pair exists for was obtained from the minimum distance d_{\min} between I^\bullet and any of the $\text{CH}_2\text{I}^\bullet$ atoms. The time traces of d_{\min} showed that the $\text{CH}_2\text{I}^\bullet + \text{I}^\bullet$ pair formed and dissociated multiple times in each of the 50 ns-simulations. To obtain the contact time of the geminate pair, we defined an event of pair formation by the criterion $d_{\min} < 0.4$ nm. Henceforth, the pair was considered as dissociated as soon as $d_{\min} > 1.2$ nm was fulfilled. This definition ensured that occasional partial dissociation of $\text{CH}_2\text{I}^\bullet$ into the second solvation shell around $\text{CH}_2\text{I}^\bullet$ followed by reformation of the pair, did not contribute to the dissociation statistics. The contact-time histogram is shown in Fig. S11(d). We estimated the bulk contact time (Fig. S12) as the 1 - the cumulative sum of the contact pair count. Subsequently, we fit a single exponential decay $f(x) = A \cdot \exp^{-x/\tau_{\text{cp}}}$ to the bulk contact time (see Fig. S12), where τ_{cp} is the contact-pair lifetime. We find that the bulk contact lifetimes for the standard GAFF force field and the force field parameterized against the results of our CASSCF-MRCI calculations are 34 ps and 204 ps, respectively.

Structural refinement against $\Delta S(q, t)$

We begin by computing the difference scattering from Eq. S6 for the candidate structures and ground state. The scattering terms are calculated for each $\text{I} \cdots \text{I}$ distance ($R_{\text{I}\cdots\text{I}}$, including the ground state $R_{\text{I}\cdots\text{I}}^{\text{gs}}$) via the equations S8, S9, and S12 as described in the previous sections. To obtain the difference scattering for the model species, we subtract the ground-state scattering from the photo-product scattering (see Fig. SS17 for the result):

$$\begin{aligned} \Delta S(R_{\text{I}\cdots\text{I}}) &= S(R_{\text{I}\cdots\text{I}}) - S(R_{\text{I}\cdots\text{I}}^{\text{gs}}) \\ \Delta S(R_{\text{I}\cdots\text{I}}) &= \Delta S_{II}(R_{\text{I}\cdots\text{I}}) + \Delta S_{SI}(R_{\text{I}\cdots\text{I}}) + \Delta S_{SS}(R_{\text{I}\cdots\text{I}}) . \end{aligned} \quad (\text{S13})$$

The heat component is already subtracted from our data. However, we include the first two or three SVD heat components to compensate for an imperfect subtraction. The total model difference scattering fit to the time-resolved WAXS data becomes

$$\begin{aligned} \Delta S_{\text{theory}}(t, q) &= \sum_m A_m(t) \cdot \Delta S(t, q, R_{\text{I}\cdots\text{I}}^m) + \sum_n h_n(t) \cdot U^{\Delta S^H}(q, n) \\ m &= \{\mathbf{GP1}; \mathbf{GP2}; \mathbf{PI}\} \quad n = \{1, 2, 3\} , \end{aligned} \quad (\text{S14})$$

with A_m as the amplitude of the photo-induced states. We impose several constraints on the structural fits: (1) The amplitudes $A_m(t)$ of each structure m are time dependent. (2) We assumed the parent molecule only adopts one ground state structure. We assume this to be the case since the negative peaks in the real-space representation of the data gives a sharp and well-defined peak at the I··I distance for the CH₂I₂. (3) The I··I distances of the photo-induced states are assumed to be constant because the atoms of these species are in equilibrium with their surroundings for delays $t > 1$ ps. The exception to this is **GP**₁, which was assumed to be time-dependent in the “ballistic regime” ($t < 500$ fs) where the position of the atoms evolve dynamically. (4) The displaced-volume form-factor scale a_{DV} (Eq. S11) was adjusted globally for all time points to a correction for the discrepancy between MD simulation and the measurement. (5) Constraints were implemented for the parameters as indicated in table S1. The optimal values for the time-dependent parameters are displayed in Fig. S16(a)-(d) and (e)-(h) for the LCLS and SACLA data, respectively.

Kinetic model of the revised reaction mechanism for the photo-dissociation of diiodomethane

Absorption of 266 nm light results in the dissociation of one of the I atoms leading to formation of a geminate pair [CH₂I• + I•], confined to one solvent cage (**GP**). There are two channels through which isomer formation can occur. The radical pair is either active (**A**) or inhibited (**In**) with respect to isomer formation. **GP** is seen in the data at two characteristic distances (denoted **GP**₁ and **GP**₂ for the peaks at $r = 4.39$ Å and $r = 5.40$ Å, respectively), where the shorter distance is formed initially and translated into the longer distance by rotational movement (k_R) of CH₂I•.

At later times rotational and translational diffusion leads to equilibration (k_{eq} and k_{-eq}). The isomer (**PI**) can only form from the active species with a recombination rate k_1 and the inhibited-active conversion rate is k_2 . We do not consider the **A** → **In** transition, since the rate constant would be much slower than the rate of isomer formation. We also model the loss of signal as a result of the parent molecule reformation rate k_{gs} . We made the assumption that the ground state recombination proceeds only via the active species. From the structural refinements, we determined that an insignificant number of I• escape the solvent cage and we therefore disregard this loss channel.

The time-dependent concentrations are described by the following set of rate equations:

$$\dot{N}_{\text{GP}_1}^{\text{A}}(t) = g - k_{\text{eq}} \cdot N_{\text{GP}_1}^{\text{A}} + k_{-\text{eq}} \cdot N_{\text{GP}_2}^{\text{A}} + k_2 \cdot N_{\text{GP}_1}^{\text{In}} - k_1 \cdot N_{\text{GP}_1}^{\text{A}} - k_{\text{gs}} \cdot N_{\text{GP}_1}^{\text{A}}, \quad (\text{S15})$$

$${}^{\text{R}}\dot{N}_{\text{GP}_1}^{\text{A}}(t) = g - k_{\text{R}} \cdot {}^{\text{R}}N_{\text{GP}_1}^{\text{A}} - k_{\text{gs}} \cdot {}^{\text{R}}N_{\text{GP}_1}^{\text{A}}, \quad (\text{S16})$$

$$\dot{N}_{\text{GP}_1}^{\text{In}}(t) = g - k_{\text{eq}} \cdot N_{\text{GP}_1}^{\text{In}} + k_{-\text{eq}} \cdot N_{\text{GP}_2}^{\text{In}} - k_2 \cdot N_{\text{GP}_1}^{\text{In}}, \quad (\text{S17})$$

$${}^{\text{R}}\dot{N}_{\text{GP}_1}^{\text{In}}(t) = g - k_{\text{R}} \cdot {}^{\text{R}}N_{\text{GP}_1}^{\text{In}}, \quad (\text{S18})$$

$$\dot{N}_{\text{GP}_2}^{\text{A}}(t) = g + k_{\text{R}} \cdot {}^{\text{R}}N_{\text{GP}_1}^{\text{A}} + k_{\text{eq}} \cdot N_{\text{GP}_1}^{\text{A}} - k_{-\text{eq}} \cdot N_{\text{GP}_2}^{\text{A}} + k_2 \cdot N_{\text{GP}_2}^{\text{In}} - k_{\text{gs}} \cdot N_{\text{GP}_2}^{\text{A}}, \quad (\text{S19})$$

$$\dot{N}_{\text{GP}_2}^{\text{In}}(t) = g + k_{\text{R}} \cdot {}^{\text{R}}N_{\text{GP}_1}^{\text{In}} + k_{\text{eq}} \cdot N_{\text{GP}_1}^{\text{In}} - k_{-\text{eq}} \cdot N_{\text{GP}_2}^{\text{In}} - k_2 \cdot N_{\text{GP}_2}^{\text{In}}, \quad (\text{S20})$$

$$\dot{N}_{\text{I}}^{\text{A}}(t) = k_1 \cdot N_{\text{GP}_1}^{\text{A}}, \quad (\text{S21})$$

$$\dot{N}_{\text{Gs}}(t) = k_{\text{gs}} \cdot (N_{\text{GP}_1}^{\text{A}} + {}^{\text{R}}N_{\text{GP}_1}^{\text{A}} + N_{\text{GP}_2}^{\text{A}}). \quad (\text{S22})$$

Where $g = \left(\frac{\phi}{\sqrt{2 \cdot \pi \cdot \sigma}} \right) \cdot \exp\left(\frac{-(t-t_0)^2}{2 \cdot \sigma^2} \right)$, with σ the pulse duration, t_0 the center of the pulse with respect to the nominal delays, and ϕ the excitation fraction. The above equations are integrated numerically to yield the time-dependent sub-populations of the **GP**₁, **GP**₂, and **PI** species. The ground state population ($N_{\text{Gs}}(t)$) is not fitted. The total populations are defined as follows:

$$\begin{aligned} N_{\text{GP}_1} &= {}^{\text{R}}N_{\text{GP}_1}^{\text{A}} + N_{\text{GP}_1}^{\text{A}} + {}^{\text{R}}N_{\text{GP}_1}^{\text{In}} + N_{\text{GP}_1}^{\text{In}} \\ N_{\text{GP}_2} &= N_{\text{GP}_2}^{\text{A}} + N_{\text{GP}_2}^{\text{In}} \\ N_{\text{I}} &= N_{\text{I}}^{\text{A}} \end{aligned} \quad (\text{S23})$$

The following parameters are defined as follows:

$$k_{-eq} = r_{eq} \cdot k_{eq} \quad (\text{S24})$$

$$N_{\text{GP}_1}^{\text{A}} = \phi \cdot r_R \quad (\text{S25})$$

$${}^R N_{\text{GP}_1}^{\text{A}} = \phi \cdot (1 - r_R) \quad (\text{S26})$$

$$N_{\text{GP}_1}^{\text{In}} = (1 - \phi) \cdot r_R \quad (\text{S27})$$

$${}^R N_{\text{GP}_1}^{\text{In}} = (1 - \phi) \cdot (1 - r_R) \quad (\text{S28})$$

$$N_{\text{GP}_2}^{\text{A}} = 0 \quad (\text{S29})$$

$$N_{\text{GP}_2}^{\text{In}} = 0 \quad (\text{S30})$$

$$N_{\text{PI}}^{\text{A}} = 0 \quad (\text{S31})$$

Where r_{eq} is the ratio between the forward and backward steady-state geminate-pair interconversion, and r_R is the fraction of rotationally excited geminate pairs. Additionally, the lag between the impulsive and kinetic regimes is modeled by shifting the time axis by a scalar $t_{i \rightarrow a}$. The results of a least-squares fit of the kinetic model to the relative amplitudes of the **GP**₁, **GP**₂, **PI** species obtained from the structural fits (table S1, and Fig. S16) are summarized in table S2.

Estimating the rotational diffusion correlation time of the **CH₂I[•]** fragment

Assuming spherical molecular envelopes, we used the Stokes-Einstein-Debye equation for rotational diffusion [38] to estimate the rotational lifetimes of molecules

$$\tau_r = \frac{\eta_m \cdot V}{k_B \cdot T} . \quad (\text{S32})$$

τ_r is the rotational correlation time of the system (s), η_m is the effective microscopic viscosity, V is the effective volume of the solvated system (m^{-3}), k_B is the Boltzmann factor ($\text{JK}^{-1} = \text{kg m}^2 \text{s}^{-2} \text{K}^{-1}$), T is the temperature (K). The effective microscopic viscosity can be calculated from the macroscopic η viscosity through micro-friction parameter γ :

$$\eta_m = \gamma \eta , \quad (\text{S33})$$

and:

$$\gamma = \left(1.5 \cdot \rho + \frac{1}{1 + \rho} \right)^{-1}, \quad \rho = \frac{r_{\text{solvent}}}{r_{\text{solute}}} . \quad (\text{S34})$$

Where r_{solvent} and r_{solute} are the radii of solvent and solute, respectively.[39–41]

Substituting: $\eta = 9.0 \times 10^{-4} \text{ kg m}^{-1} \text{ s}^{-1}$ [39], $V = \frac{4}{3}\pi r_{\text{solute}}^3$, $r_{\text{solute}} = 0.336 \text{ nm}$ (half the radius of gyration estimated with the python MDAnalysis module [42, 43] from a $\text{CH}_2\text{I}^\bullet$ fragment built with Avogadro [44]), $r_{\text{solvent}} = 0.368 \text{ nm}$, $T = 298 \text{ K}^{-1}$ yields

$$\tau_r = \frac{4.25 \times 10^{-4} \cdot 1.59 \times 10^{-28}}{1.3806488 \times 10^{-23} \cdot 298} = 16.4 \text{ ps} . \quad (\text{S35})$$

Estimating the translational and rotational kinetic energy of the $\text{CH}_2\text{I}^\bullet$ and I^\bullet fragments

We used the following to calculate the translational and rotational kinetic energy from the trajectories of the photofragments.

Translational Kinetic Energy - The translational kinetic energy for a single dissociating molecule is given by:

$$E_K^T = 1/2 \cdot \mu \cdot v_{\text{obs}}^2 , \quad (\text{S36})$$

with the reduced mass $\mu = \frac{(m_1 \cdot m_2)}{(m_1 + m_2)}$, and observed velocity of the fragments v_{obs} . The mass of the $\text{CH}_2\text{I}^\bullet$ fragment m_1 is $2.34 \times 10^{-25} \text{ kg}$ and the mass of the I^\bullet fragment m_2 is $2.11 \times 10^{-25} \text{ kg}$. We obtain $\mu = 1.11 \times 10^{-25} \text{ kg}$ and $v_{\text{obs}} = 213 \text{ m s}^{-1}$. The translational kinetic energy per mole of $\text{CH}_2\text{I}^\bullet$ is calculated by multiplying E_K^T with Avogadro's number:

$$E_K^T = 0.5 \cdot 1.11 \times 10^{-25} \cdot 213^2 \cdot 6.02214076 \times 10^{23} \cdot 1 \times 10^{-3} = 1.51 \text{ kJ mol}^{-1} . \quad (\text{S37})$$

Rotational Kinetic Energy - The rotational kinetic energy for a single dissociating molecule is given by:

$$E_K^R = 1/2 \cdot I \cdot \omega^2 , \quad (\text{S38})$$

where the moment of inertia I and the angular velocity of the rotor ω can be rewritten as $m * r^2$

and $2 \cdot \pi \cdot f$, respectively:

$$E_K^R = 1/2 \cdot m \cdot r^2 \cdot (2 \cdot \pi \cdot f)^2, \quad (\text{S39})$$

The frequency of the rotation is obtained from the measured rotational excitation rate as follows: $f = \frac{k_R}{2} \cdot 1 \times 10^{12} \text{ s}^{-1}$. The rate of rotational excitation k_R is observed through the fast conversion of the geminate pair I...I distances from $R_{I...I} = 4.4 \text{ \AA} \rightarrow 5.4 \text{ \AA}$. Therefore, k_R represents a half-rotation of the CH_2 moiety around the I atom (which is the axis of rotation due to its significantly superior mass). The angular velocity is defined as the number of rotations per second, which is half the measured rate k_R . The rotating mass m of the fragment is $2.34 \times 10^{-26} \text{ kg}$. The radius of gyration of the $\text{CH}_2\text{I}^\bullet$ fragment is 0.672 nm (see the treatment of the rotational correlation lifetime of the $\text{CH}_2\text{I}^\bullet$ above) with the I atom as the center of the rotation. The rotational kinetic energy per mole of $\text{CH}_2\text{I}^\bullet$ is calculated by multiplying E_K^R with Avogadro's number:

$$\begin{aligned} E_K^R &= 1/2 \cdot 2.34 \times 10^{-26} \cdot 0.672^2 \cdot (\pi \cdot 1.3 \times 10^{12})^2 \cdot 6.022 \ 140 \ 76 \times 10^{23} \cdot 1 \times 10^{-3} \\ &= 52.7 \text{ kJ mol}^{-1}. \end{aligned} \quad (\text{S40})$$

Systematic evaluation of the considered chemical species in the modelling of the difference scattering

We investigated the importance of the geminate pair and the solvent separated species to describe the difference scattering data (see main text Fig. 2). Model 1 includes the geminate pair (both $R_{I...I} = 4.39 \text{ \AA}$ and $R_{I...I} = 5.40 \text{ \AA}$ distances), the isomer, and a solvent-separated pair (s. sep. $R_{I...I} = 100 \text{ \AA}$). Model 1 is used in the data analysis discussed in the main text (see main text Fig. 1). Model 2 is comprised of the geminate pair and the isomer. Model 3 includes the solvent separated species and the isomer. (see Supporting Information Fig. S18). The best agreement between model and data is obtained for model 1 ($\chi^2 = 626$) (panels (a)-(c)). The solvent-separated pair is observed for some time points (Panel (a)). Model 2 has a similar agreement with the data ($\chi^2 = 626$) (panels (d)-(f)). Finally, model 3 has a significantly worse agreement with the data ($\chi^2 = 1090$) (panels (g)-(i)). The analysis shows that a the radical pair within the same solvent shell has to be included to reproduce the data on the timescale of hundreds of picoseconds.

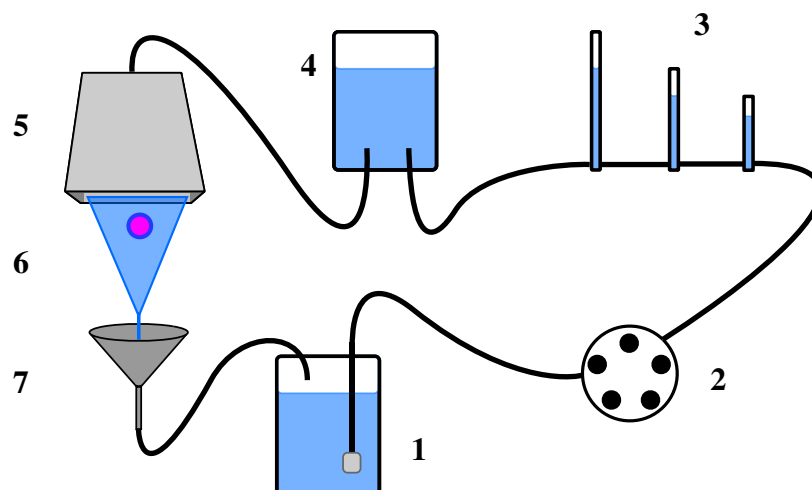


FIG. S1. Schematic diagram of the sample-delivery system used at SACLA and for the transient absorption measurements. The connecting tubes are indicated by solid lines. The liquid flows in the same direction as the components in ascending order. The labeled components are not to scale. The sample solution was kept in a reservoir (200 ml GL-45 glass bottle, **1**). The intake tube was fitted with an HPLC filter ($1/16''$ inlet, $20\ \mu\text{m}$ porosity, Gilson) to prevent the system from clogging downstream. The solution was recirculated using a peristaltic pump (Masterflex L/S Modular Drive & Easy-Load II pump head, Cole-Parmer, **2**) with chemically resistant tubing (Fluran F5500 $1/8''$ inner diameter, Saint-Gobain; Chemflur PTFE, $1/8'' \times 1/4''$, Cole-Parmer) and PFA/PTFE fittings (Cole-Parmer and IDEX). The pulsations of the peristaltic pump were eliminated by running the pump at 60 rpm with a low occlusion volume followed by a combination of three varying-volume air traps (**3**) and a compression chamber (100 ml GL-45 glass bottle fitted with a three-port sealed PTFE cap, Omnifit, **4**). A liquid-sheet jet ($100\ \mu\text{m}$ thick, **6**) was achieved by running the sample solution through a hollow rectangular capillary with an inner geometry of $100\ \mu\text{m} \times 2\ \text{mm}$ (borosilicate glass, VitroCOM, **5**). At the LCLS a round jet ($50\ \mu\text{m}$ diameter) was used. The expended liquid was captured by a glass funnel (**7**) and delivered back to the reservoir. The total liquid volume necessary to run the system was 500 ml.

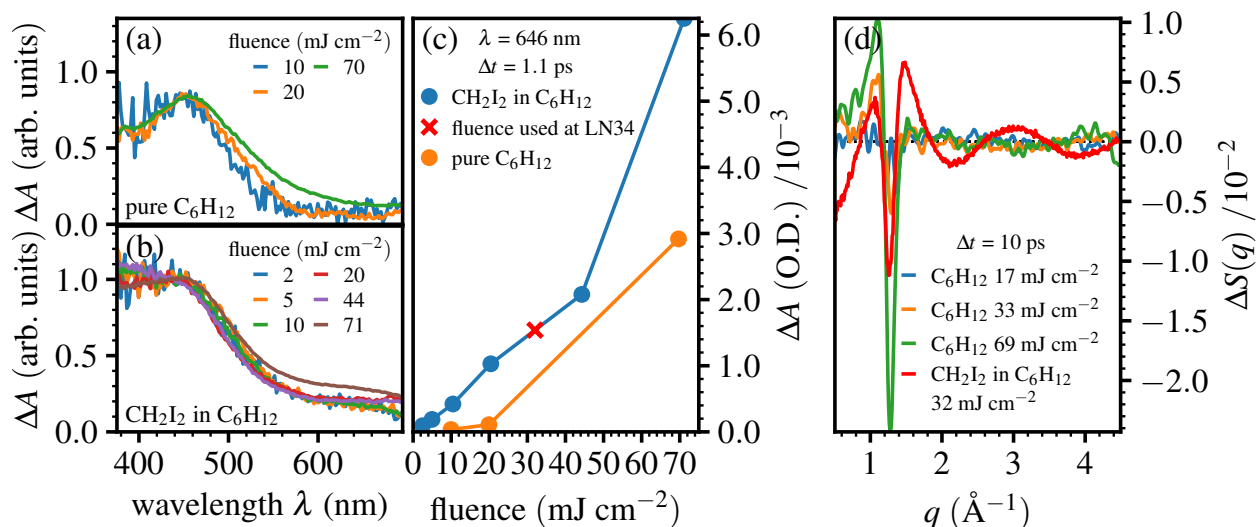


FIG. S2. Difference-WAXS and transient-absorption signal laser-fluence dependence. (a) Change in absorption (ΔA) 1.1 ps after laser excitation of pure cyclohexane excited at 266 nm. (b) ΔA of CH_2I_2 in cyclohexane at 1.1 ps after laser excitation excited at 266 nm for different laser fluences. The signals in panels a and b are on the same, but arbitrary scale. (c) ΔA at 646 nm extracted from the data shown in panels a and b as a function of laser fluence. The absorption at this wavelength is predominantly caused by the fragments of the photodissociation. (d) Difference scattering ($\Delta S(q)$) of cyclohexane and CH_2I_2 10 ps after laser excitation excited at 266 nm for different laser fluences. The oscillating signal at around $1.3\ \text{\AA}^{-1}$ is due to solvent heating. The pump-pulse length for the difference-WAXS and transient-absorption power dependence are 60 fs and 80 fs (FWHM) respectively.

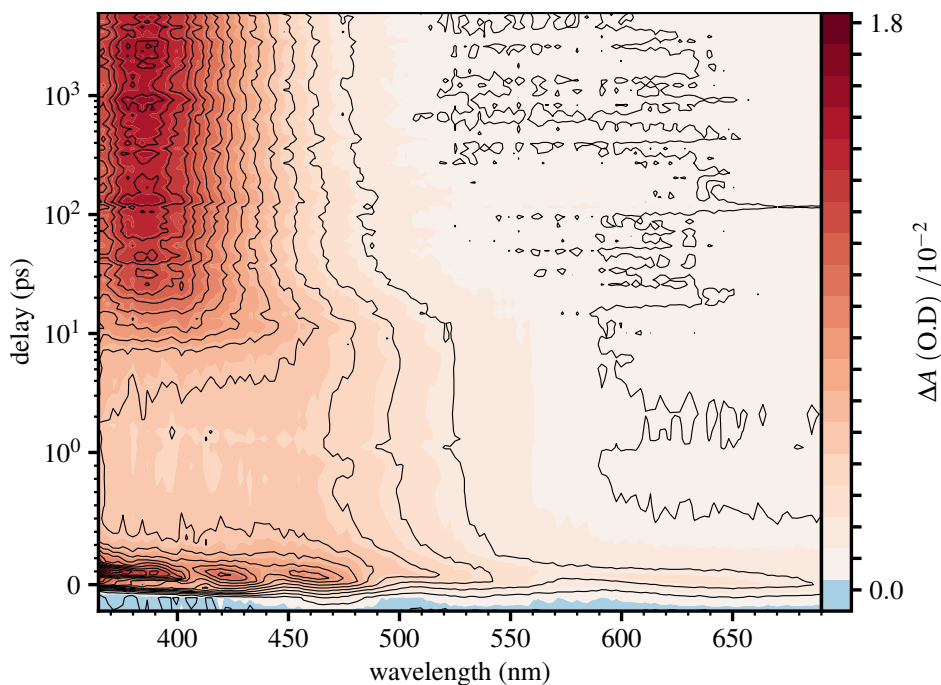


FIG. S3. The transient-absorption spectra of the photodissociation of diiodomethane in cyclohexane in the range of -5 ps to 5000 ps with a $20\ mJ\ cm^{-2}$ excitation fluence.

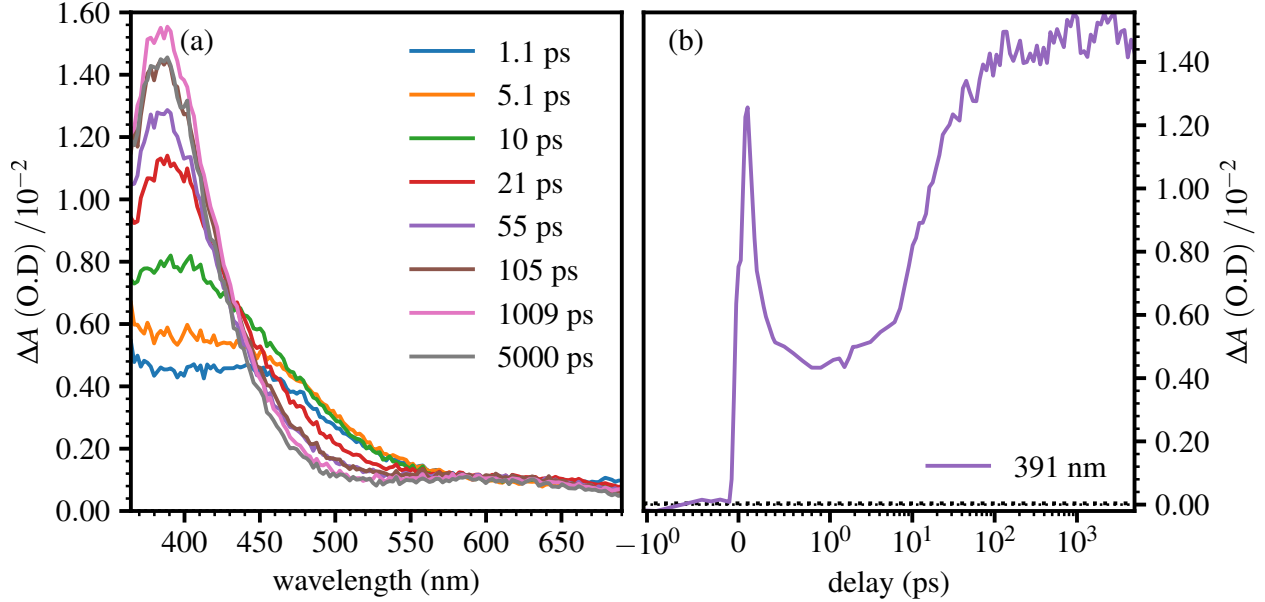


FIG. S4. Different representations of the transient absorption of the photodissociation of diiodomethane in cyclohexane. (a) transient absorption spectra at selected delay times after 20.4 mJ cm^{-2} excitation. (b) normalized difference absorption at 392 nm as a function of delay after excitation at different excitation fluences.

TABLE S1. Summary of the time-independent parameters used to fit the WAXS data of run LN34 (Fig. S13) and 2016A8037 (Fig. S14). Time-dependent parameters (varied at each delay value) are summarized in Fig. S16(a) and (b). “cnstr. min.” and “cnstr. max.” respectively stand for the minimum and maximum values that the variable was allowed to take. ^a time-independent for $t > 0.5 \text{ ps}$.

variable	run LN34	run 2016A8037	cnstr. min.	cnstr. max.
	value $\pm 1\sigma$ error	value $\pm 1\sigma$ error		
t_0 (ps)	0.23 ± 0.01	0.06 ± 0.01	0.0	0.4
t_s (ps)	-1.40 ± 0.07	-0.7 ± 0.2	0.0	-1.0
$I \cdots I_{free\ flight}$ (ps)	0.34 ± 0.07	1.1 ± 0.2	0.0	0.4
$I \cdots I_{velocity}$ (\AA ps^{-1})	2.1 ± 0.4	0.7 ± 0.1	N.A.	N.A.
a_{DV}	1.15 ± 0.02	1.71 ± 0.02	0.1	2.5
$R_{I \cdots I}^{GS}$ (\AA)	3.62 ± 0.01	3.63 (fixed)	N.A.	N.A.
^a $R_{I \cdots I}^{GP1}$ (\AA)	4.35 ± 0.03	4.40 ± 0.01	3.3	5.0
$R_{I \cdots I}^{GP2}$ (\AA)	5.40 ± 0.02	5.26 ± 0.02	5.0	5.9
$R_{I \cdots I}^{PI}$ (\AA)	3.13 ± 0.04	2.77 ± 0.02	2.1	3.4

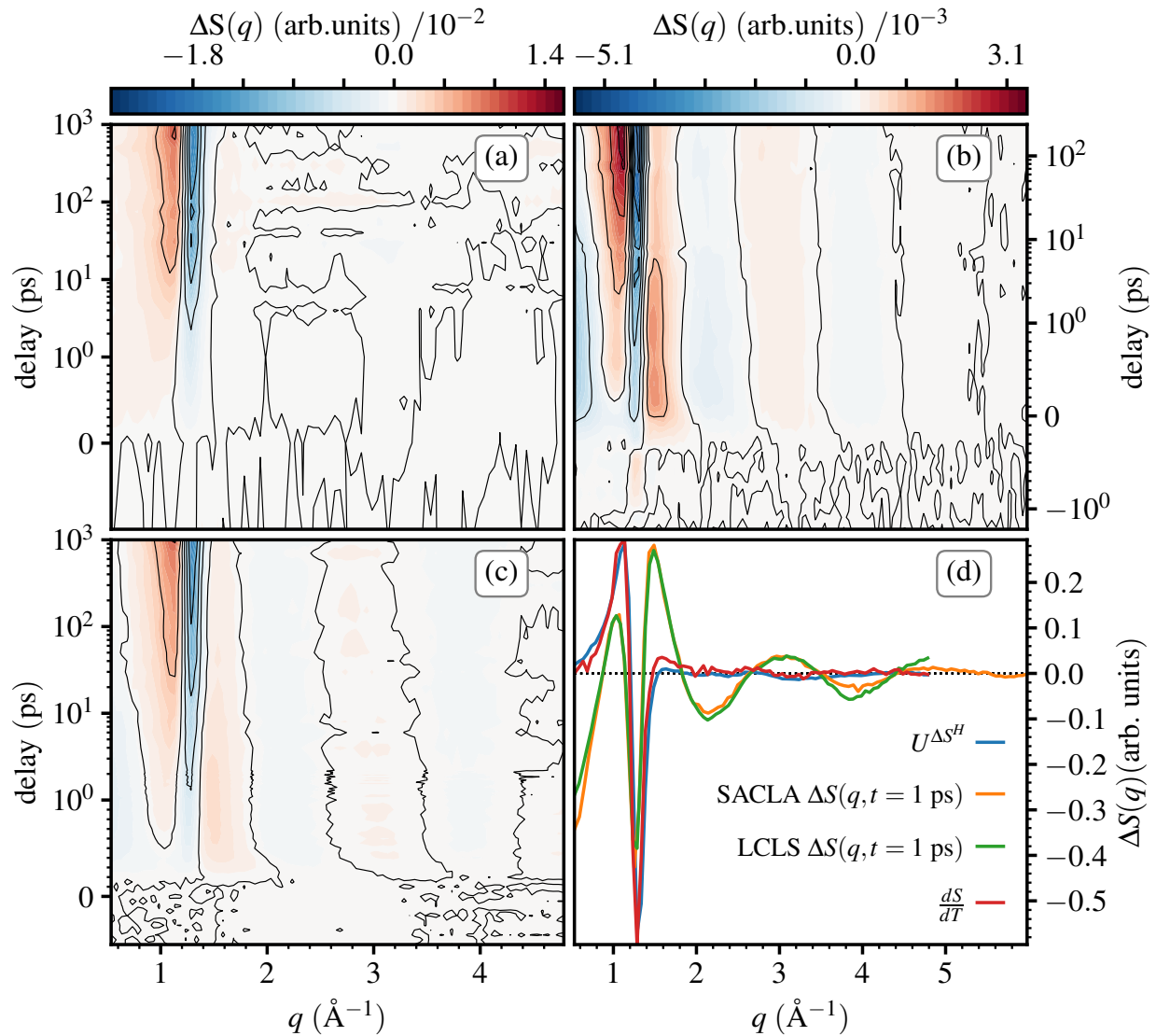


FIG. S5. Comparison of the difference scattering recorded at SACLA and the LCLS before heat subtraction. (a) Difference scattering ($\Delta S(q)$) of the heat dye as a function of delay after laser excitation and momentum transfer (q) measured in run LN34 at the LCLS. (b) Difference scattering ($\Delta S(q)$) of the photodissociation CH_2I_2 as a function of delay after laser excitation in reciprocal space (q) measured in run 2016A8037 at SACLA. (c) Difference scattering ($\Delta S(q)$) of the photodissociation CH_2I_2 as a function of delay after laser excitation in reciprocal space (q) measured in run LN34 at the LCLS. (d) Comparison of the 1st projection vector of an SVD of the data $U^{\Delta S^H}$ in panel a, the difference scattering at 1 ps after laser excitation measured during the LCLS and SACLA runs, and the time-independent heat-response (differential) of cyclohexane measured using synchrotron radiation in Ref. [1]. The curves are normalized to the square root of the absolute squares of the difference scattering.

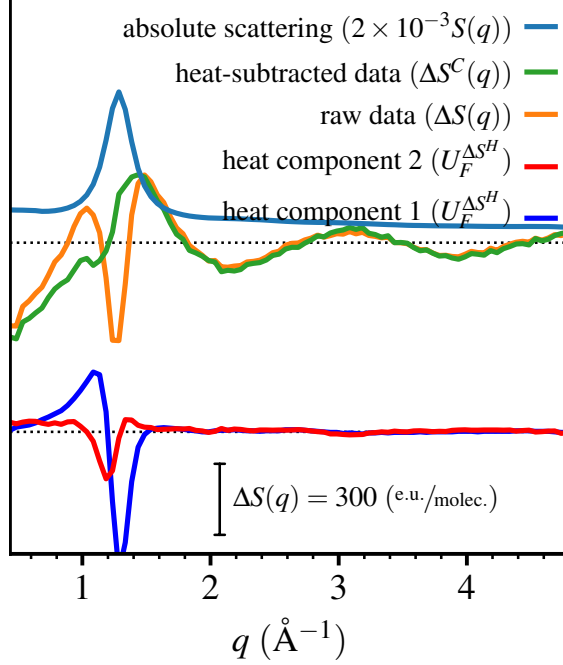


FIG. S6. Demonstration of the heat-subtraction procedure at 1 ps. The raw data, heat-subtracted data, first and second SVD projection vectors of the solvent heat-response are shown. The sum of the SVD components are subtracted from the raw data to yield the heat-subtracted data. The determination of the amplitudes of the SVD-components is summarized in Fig. S7.

TABLE S2. Summary of parameters obtained from the least-squares fit of the kinetic model to the amplitudes of the **GP**₁, **GP**₂, **PI** species. The amplitudes are shown in (Fig. S13 (LCLS)). The least-squares fit are shown in main-text Fig. 2(a).

run LN34	
variable	value $\pm 1\sigma$ error
N^{Exc}	0.157 ± 0.002
$\sigma_{\text{I.r.f.}}$ (ps)	0.08 ± 0.01
r_{eq}	0.71 ± 0.02
k_R (ps ⁻¹)	1.3 ± 0.1
k_{eq} (ps ⁻¹)	1.5 ± 0.3
k_1 (ps ⁻¹)	0.12 ± 0.02
k_2 (ns ⁻¹)	0.35 ± 0.70
χ^A	0.33 ± 0.02
k_{-eq} (ps ⁻¹)	2.1 ± 0.4

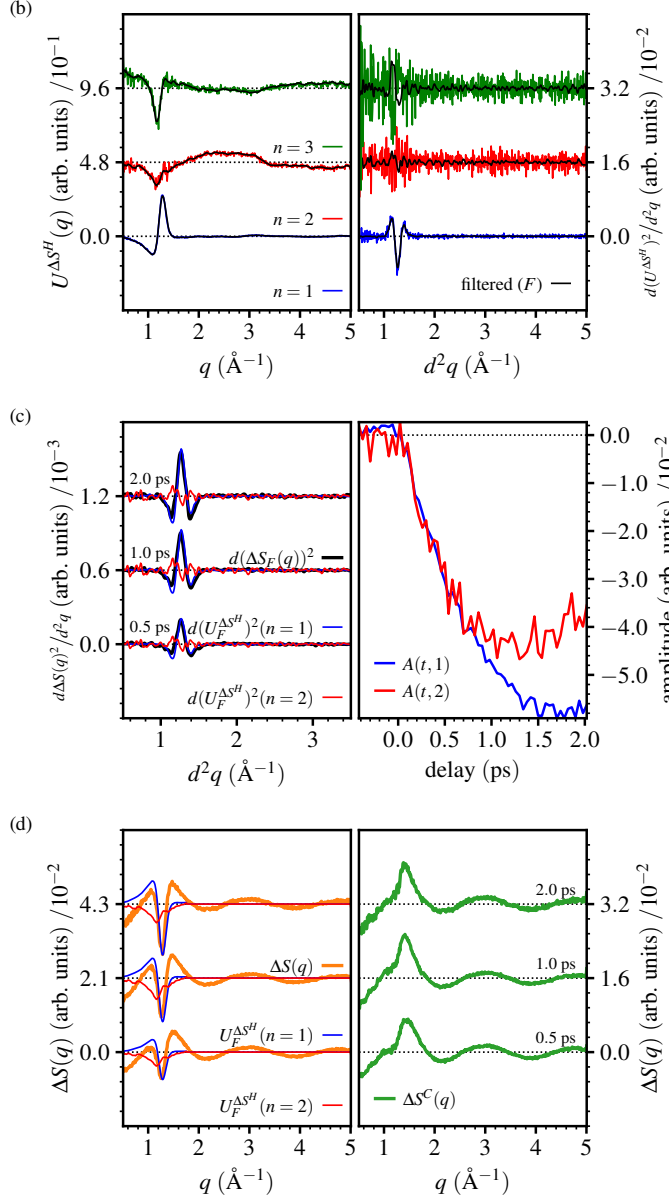
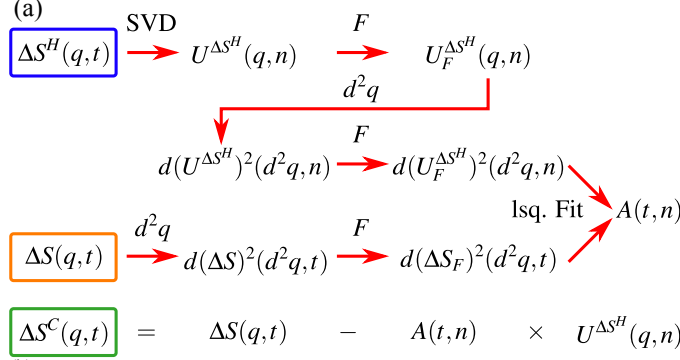


FIG. S7. Overview of the heat-subtraction method. (a) Schematic representation of the heat-subtraction method. Data processing flow chart where SVD stands for Singular Value Decomposition, F stands for filtering, d^2q is taking the 2nd derivative along the scattering vector q , and “lsq. Fit” stands for least squares fit. The blue and yellow boxes mark the measured input data, and the green box marks the corrected output data, which is shown in Fig. 1. (b) First three projection vectors obtained from an SVD of the heat response ($U^{\Delta S^H}$, left) and the second derivatives ($d(U^{\Delta S^H})^2/d^2q$, right). The black lines represent the smoothed (filtered) curves. (c) 2nd derivative of the data ($d(\Delta S_F(q))^2/d^2q$) at three delays ($t = 0.5, 1.0, 2.0$ ps) are shown together with the contributions of first two SVD components ($d(U^{\Delta S^H})^2/d^2q$) at each delay (left). Contributions $A(t, n)$ of the first two projection vectors determined from a least squares fit are shown as a function of t (right). (d) The data ($\Delta S(q)$) at three delays ($t = 0.5, 1.0, 2.0$ ps) and the contributions of first two SVD components ($U^{\Delta S^H}$) at each delay determined from the least squares fit (left). Corrected difference-scattering curves ($\Delta S^C(q)$) obtained by subtracting $U^{\Delta S^H}(q, n = 1, 2) \times A(t = 0.5, 1.0, 2.0 \text{ ps}, n = 1, 2)$ from $\Delta S(q, t = 0.5, 1.0, 2.0 \text{ ps})$.

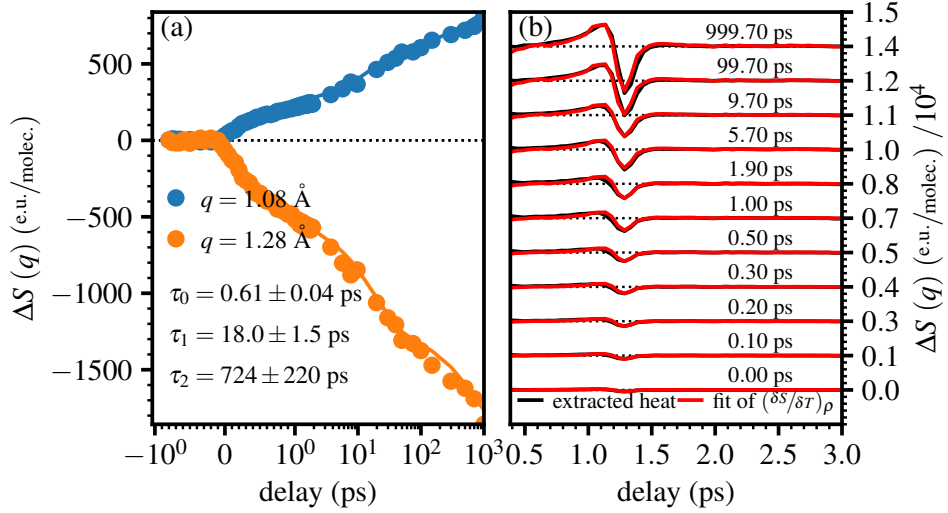


FIG. S8. (a) reconstructed heat signal from the three SVD components used in the heat subtraction of the difference scattering data (red) and least-squares fit of the published cyclohexane difference-scattering signal at constant density $(\delta S / \delta T)_\rho$. (b) time dependence of the reconstructed heat signal and model at the maximum and minimum momentum transfer (q) of the signals. Three lifetimes (reported in (b)) were necessary to model the data.

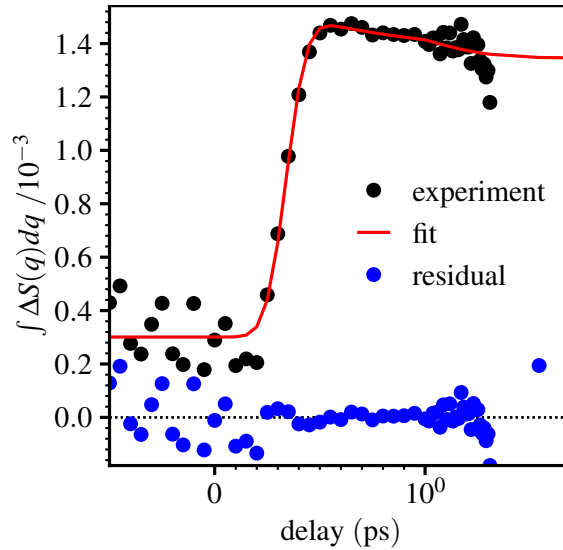


FIG. S9. Determination of the instrument response function (IRF) from the integrated difference scattering over a q -range spanning 2 \AA^{-1} to 4.5 \AA^{-1} of the LN34 experiment.

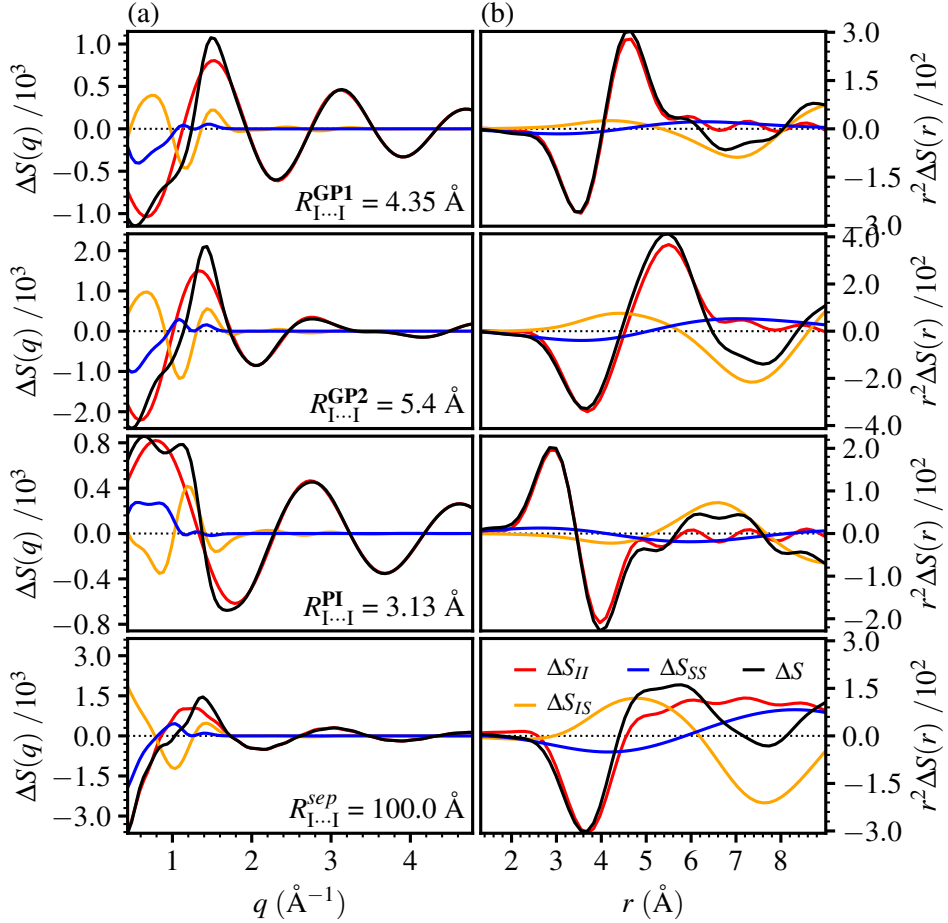


FIG. S10. **Calculated difference scattering contributions of the photo-products.** (a) Calculated difference scattering ($\Delta S(q)$) of different $R_{I...I}$ distances corresponding to those of the **GP**₁, **GP**₂, **PI**, and the solvent-separated pair (labeled in the plot) in reciprocal space (q). (b) Real-space representation (r) of the difference scattering ($r^2\Delta S(r)$) obtained by a sine-Fourier transformation of the curves shown in panel a. Red, orange, blue, and black lines indicate the solute ΔS_{II} (Eq. S8), solvent cage ΔS_{IS} (Eq. S9), solvent-only scattering ΔS_{SS} (Eq. S12), and the total scattering ΔS respectively.

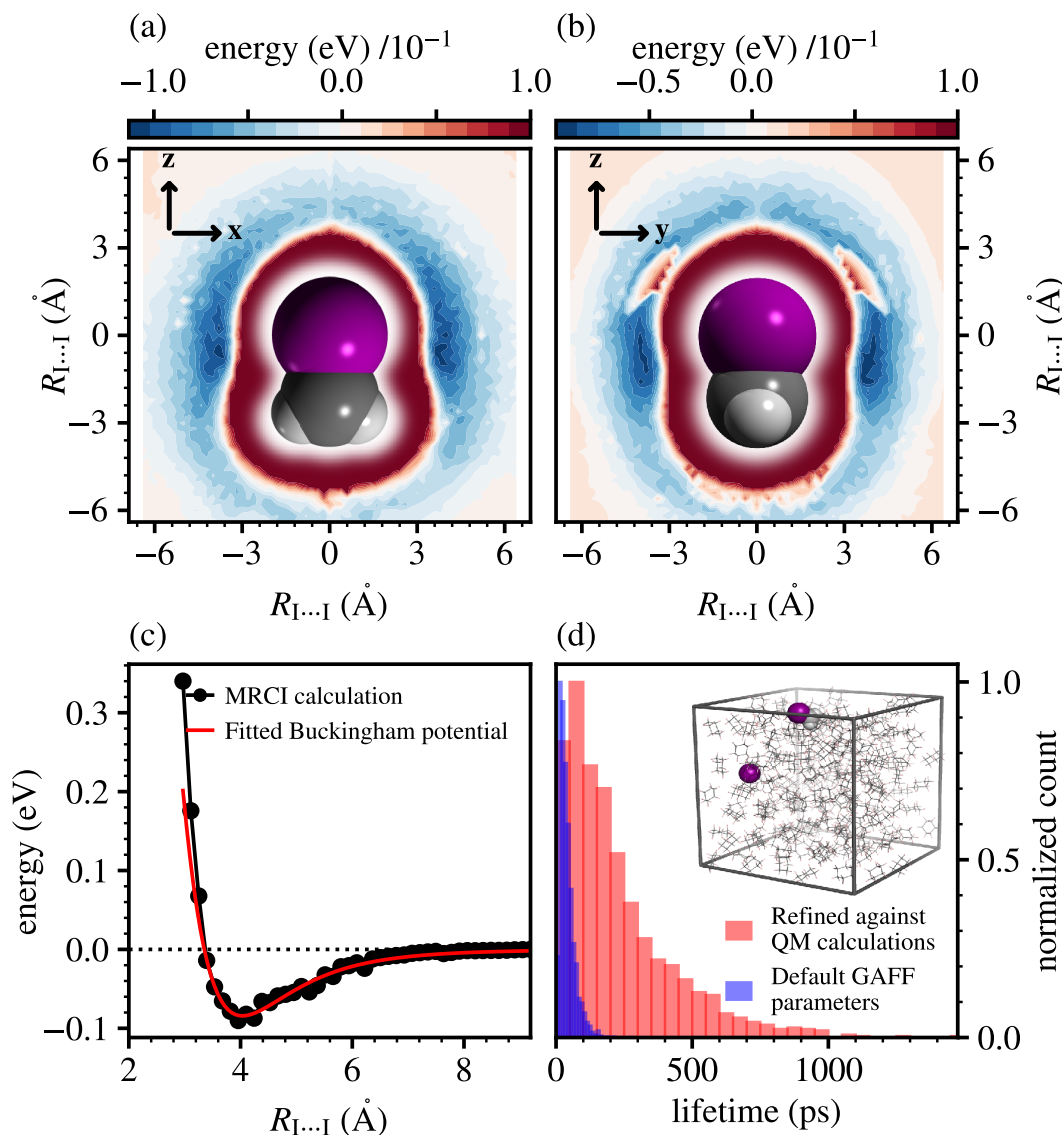


FIG. S11. $I\cdots I$ potential energy surfaces obtained from QM calculations of the $I\bullet + CH_2I\bullet$ pair in cyclohexane and summary of the MD simulation results with the $I\cdots I$ potential parameterized against quantum-chemical calculations. The coordinate (0,0) marks the center of the parent molecule I atom. (a) two-dimensional slice of the potential energy surface in the x - z plane. (b) two-dimensional slice of the potential energy surface in the y - z Plane. (c) Black dots: Potential energy scan between the $I\bullet$ and $CH_2I\bullet$ fragments from quantum-chemical calculations, revealing considerable dispersive interactions. Red: Fitted Buckingham potential used during MD simulation. (d) lifetime histogram of the $CH_2I\bullet + I\bullet$ pair obtained from the classical MD simulations with a Buckingham potential refined against the QM calculations and default GAFF parameters. Inset: Snapshot of an MD simulation of a system comprising $CH_2I\bullet$ and $I\bullet$ (spheres) in cyclohexane (sticks).

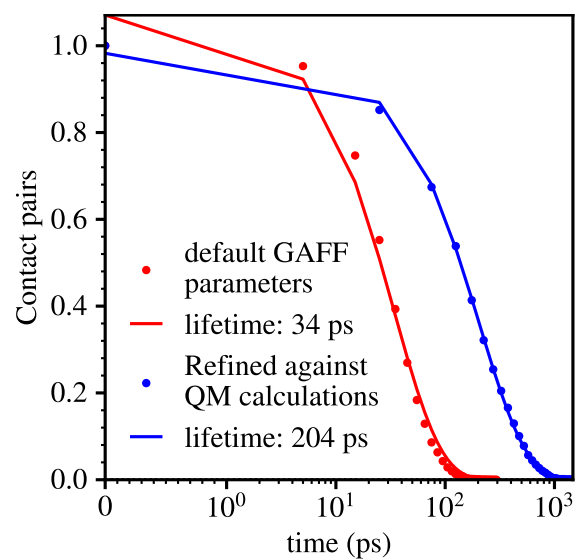


FIG. S12. Contact pairs as a function of time determined from MD simulations with the standard GAFF force field and parameterized against the results of the CASSCF-MRCI calculations.

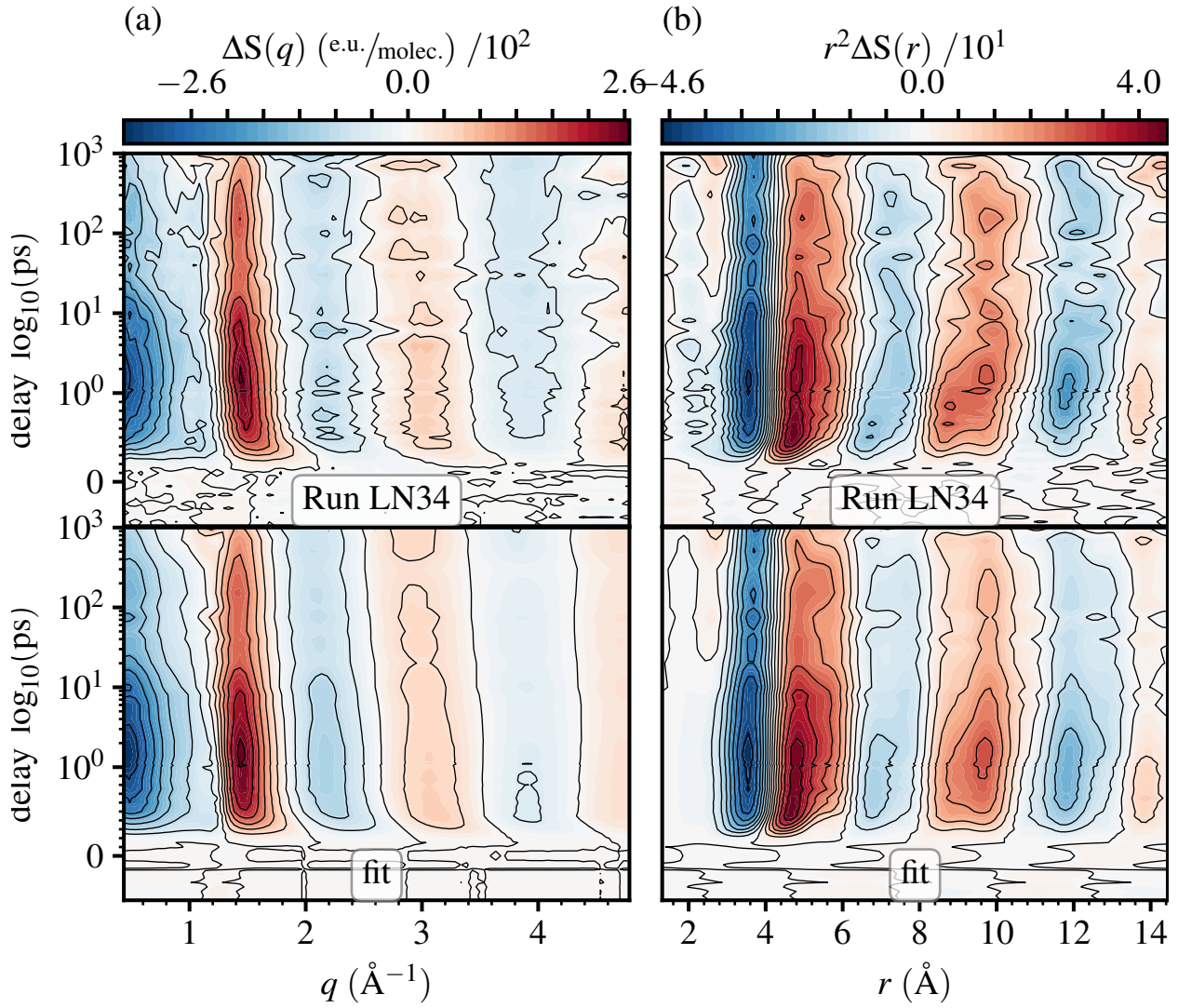


FIG. S13. Overview of the data and structural fits from run LN34 at the LCLS. (a) Measured difference scattering (top, $\Delta S(q)$) and structural least-squares fit (bottom) at different delays after laser excitation in reciprocal space (q). (b) Real-space representation (r) of the difference scattering ($r^2\Delta S(r)$) and structural fits obtained by a sine-Fourier transformation of the data shown in panel a. The experimental data have been filtered using a low-pass Fourier filter.

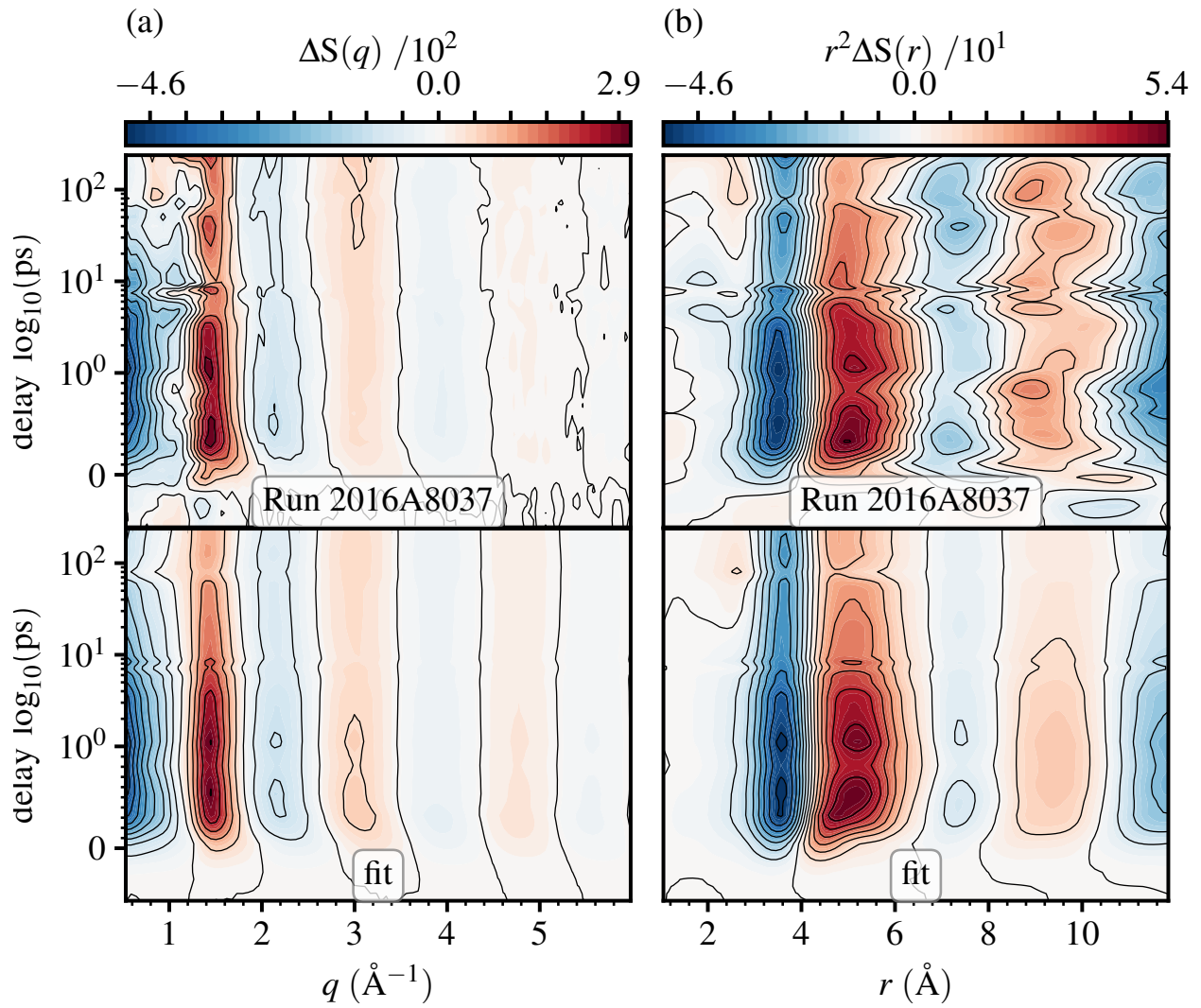


FIG. S14. Overview of the data and structural fits from run 2016A8037 at SACLA. (a) Measured difference scattering (top, $\Delta S(q)$) and structural least-squares fit (bottom) at different delays after laser excitation in reciprocal space (q). (b) Real-space representation (r) of the difference scattering ($r^2 \Delta S(r)$) and structural fits obtained by a sine-Fourier transformation of the data shown in panel a. The experimental data have been filtered using a low-pass Fourier filter.

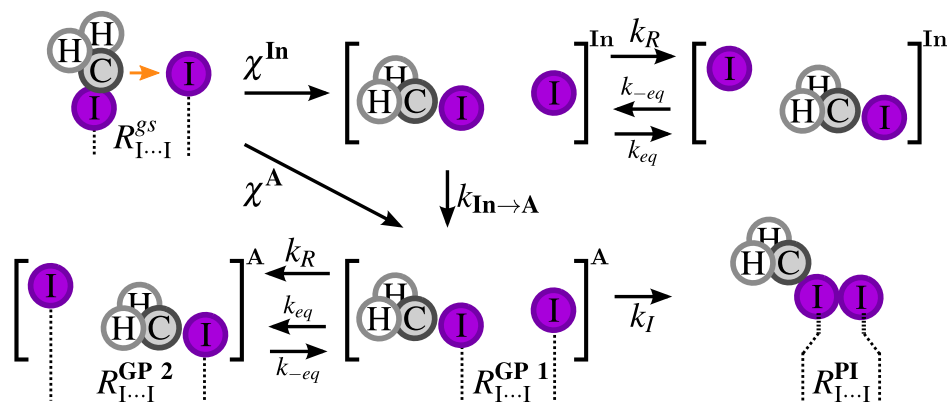


FIG. S15. Revised reaction scheme of the photodissociation of diiodomethane. Schematic representation of the kinetic model described by equations S15-S31. χ^A and χ^{In} are the fractions of the total active and inhibited species, respectively.

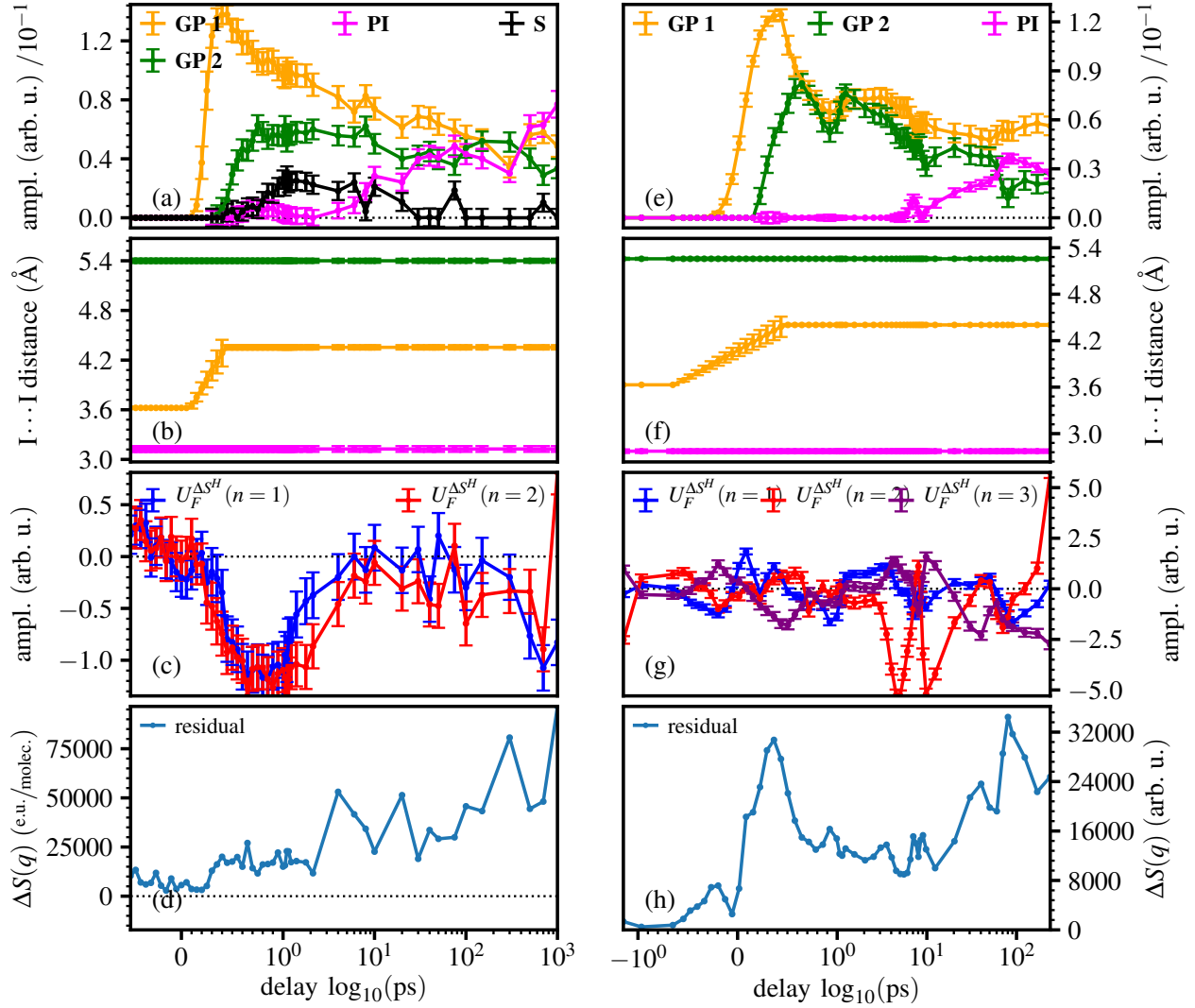


FIG. S16. Summary of the time-dependent fit parameters and residuals of the kinetic model for run LN34 (panels (a)-(d)) and run 2016A8037 (panels (e)-(h)). (a) and (e) amplitudes of the different species. The colors of the **GP**₁, **GP**₂, **PI**, solvent separated pair (**S**) correspond to those in Fig. 1 and 2 in the main text. (b) and (f) I...I distances of the **GP**₁, **GP**₂, and **PI**. The I...I distance of **GP**₁ is time-dependent for $t \leq 1$ ps, **GP**₂ and **PI** I...I distances are shown as a reference. (c) and (g) amplitudes of the heat components. The solvent SVD components, $U_F^{\Delta S^H}$, correspond to Fig. S7(b) left panel. (d) and (h) sum of the residuals of the structural fit, Fig. S13 and S14, at each delay after the laser excitation. The error bars represent a 1σ standard deviation obtained from the least-squares fit.

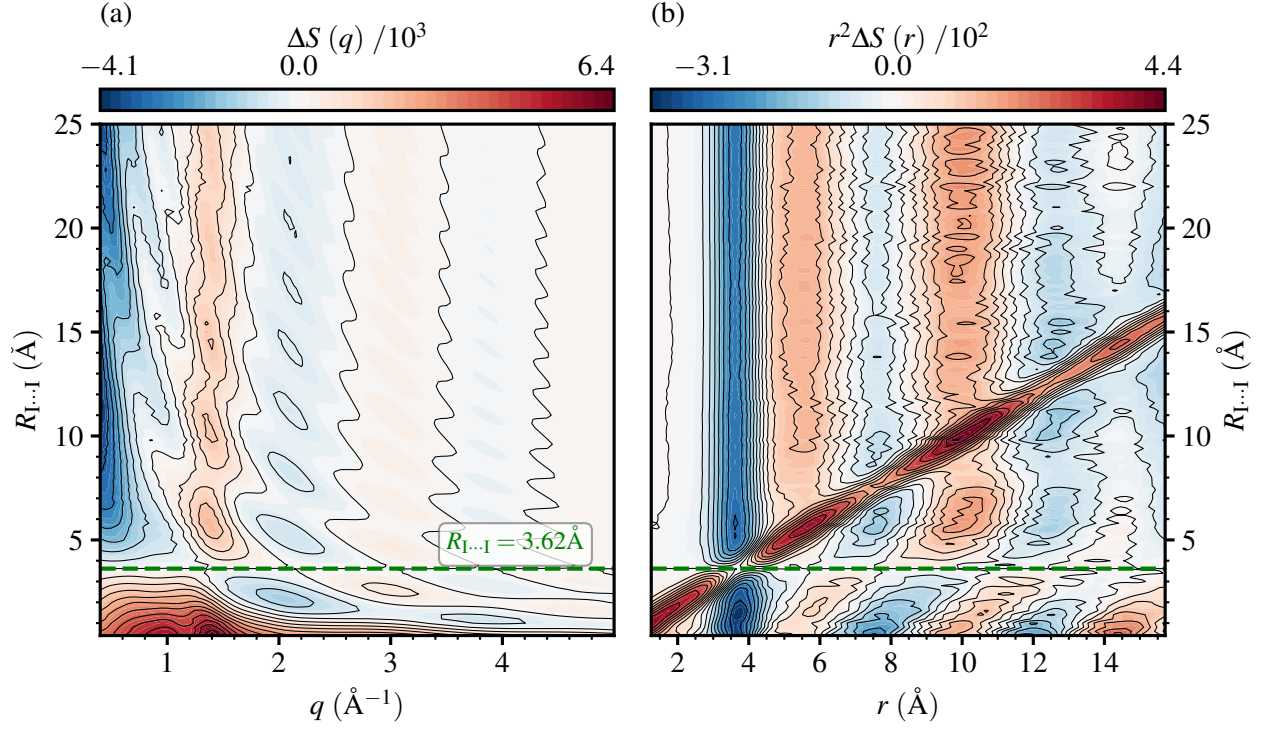


FIG. S17. The 124 scattering profiles used to fit the time-dependent scattering data. The figure shows a contour plot of the total difference scattering (Eq. S13 in the main text) of the 124 models used in q -space and the sine-Fourier transform (real-space) versus I...I distance ($R_{I...I}$). The curves are generated by subtracting the absolute scattering of the structure representing the ground state distance of 3.62 Å (marked with a green dashed line) from the absolute scattering of the other structures.

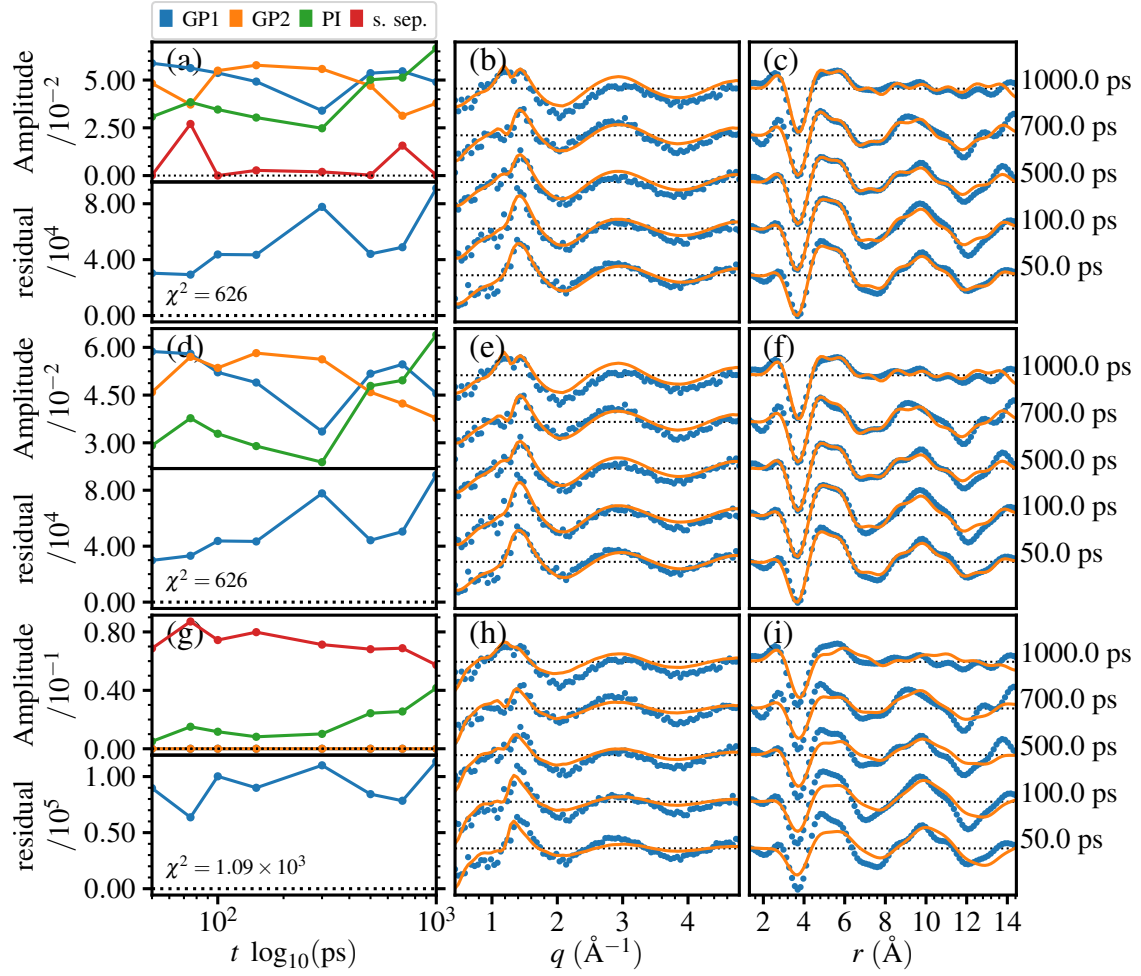


FIG. S18. Comparison of different setups for the structural fits. The figure shows the time dependence of the optimal amplitudes of each state (left), the fits (lines) and data (dots, LCLS) in q -space (middle) and in r -space (right), obtained by sine-Fourier transform of the corresponding data set in q .

* westenho@chem.gu.se

† Current affiliation: PULSE Institute, SLAC National Laboratory, Menlo Park, California 94305, USA

- [1] K. S. Kjaer, T. B. van Driel, J. Kehres, K. Haldrup, D. Khakhulin, K. Bechgaard, M. Cammarata, M. Wulff, T. J. Sorensen, and M. M. Nielsen, Introducing a standard method for experimental determination of the solvent response in laser pump, X-ray probe time-resolved wide-angle X-ray scattering experiments on systems in solution, *Phys. Chem. Chem. Phys.* **15**, 15003 (2013).
- [2] M. Chollet, R. Alonso-Mori, M. Cammarata, D. Damiani, J. Defever, J. T. Delor, Y. Feng, J. M. Glow-
nia, J. B. Langton, S. Nelson, K. Ramsey, A. Robert, M. Sikorski, S. Song, D. Stefanescu, V. Srinivasan, D. Zhu, H. T. Lemke, and D. M. Fritz, The X-ray Pump–Probe instrument at the Linac Coherent Light Source, *J. Synchrotron Radiat.* **22**, 503 (2015).
- [3] K. Tono, Y. Inubushi, T. Sato, T. Togashi, H. Ohashi, H. Kimura, S. Takahashi, K. Takeshita, H. Tomizawa, S. Goto, and M. Yabashi, Beamline for X-ray free electron laser of SACLA, *J. Phys. Conf. Ser.* **425**, 072006 (2013).
- [4] M. P. Minitti, J. S. Robinson, R. N. Coffee, S. Edstrom, S. Gilevich, J. M. Glow-
nia, E. Granados, P. Hering, M. C. Hoffmann, A. Miahnahri, D. Milathianaki, W. Polzin, D. Ratner, F. Tavella, S. Vetter, M. Welch, W. E. White, and A. R. Fry, Optical laser systems at the Linac Coherent Light Source, *J. Synchrotron Radiat.* **22**, 526 (2015).
- [5] M. Harmand, R. Coffee, M. Bionta, M. Chollet, D. French, D. Zhu, D. Fritz, H. Lemke, N. Medvedev, B. Ziaja, S. Toleikis, and M. Cammarata, Achieving few-femtosecond time-sorting at hard X-ray free-electron lasers, *Nat. Photon.* **7**, 215 (2013).
- [6] K. Tono, T. Togashi, Y. Inubushi, T. Sato, T. Katayama, K. Ogawa, H. Ohashi, H. Kimura, S. Takahashi, K. Takeshita, H. Tomizawa, S. Goto, T. Ishikawa, and M. Yabashi, Beamline, experimental stations and photon beam diagnostics for the hard X-ray free electron laser of SACLA, *New J. Phys.* **15**, 083035 (2013).
- [7] T. Sato, T. Togashi, K. Ogawa, T. Katayama, Y. Inubushi, K. Tono, and M. Yabashi, Highly efficient arrival timing diagnostics for femtosecond X-ray and optical laser pulses, *Appl. Phys. Express* **8**, 012702 (2015).
- [8] T. Katayama, S. Owada, T. Togashi, K. Ogawa, P. Karvinen, I. Vartiainen, A. Eronen, C. David, T. Sato, K. Nakajima, Y. Joti, H. Yumoto, H. Ohashi, and M. Yabashi, A beam branching method for

- timing and spectral characterization of hard X-ray free-electron lasers, *Struct. Dyn.* **3**, 034301 (2016).
- [9] T. Sato, T. Togashi, K. Tono, Y. Inubushi, H. Tomizawa, Y. Tanaka, S. Adachi, K. Nakamura, R. Kodama, and M. Yabashi, Development of ultrafast pump and probe experimental system at SACLA, *J. Phys. Conf. Ser.* **425**, 092009 (2013).
- [10] B. J. Schwartz, J. C. King, J. Z. Zhang, and C. B. Harris, Direct femtosecond measurements of single collision dominated geminate recombination times of small molecules in liquids, *Chem. Phys. Lett.* **203**, 503 (1993).
- [11] K.-I. Saitow, Y. Naitoh, K. Tominaga, and K. Yoshihara, Photo-induced reactions of CH_2I_2 in solution studied by the ultrafast transient absorption spectroscopy, *Chem. Phys. Lett.* **262**, 621 (1996).
- [12] A. N. Tarnovsky, V. Sundström, E. Åkesson, and T. Pascher, Photochemistry of Diiodomethane in Solution Studied by Femtosecond and Nanosecond Laser Photolysis. Formation and Dark Reactions of the $\text{CH}_2\text{I-I}$ Isomer Photoproduct and Its Role in Cyclopropanation of Olefins, *J. Phys. Chem. A* **108**, 237 (2004).
- [13] Y.-L. Li, D. Wang, and D. L. Phillips, Time-resolved resonance Raman spectroscopy and density functional theory investigation of the $\text{CH}_2\text{I-I}$ isomer and $\text{CH}_2\text{I}_2 \cdots \text{I}$ molecular complex products produced from ultraviolet photolysis of CH_2I_2 in the solution phase: Comparison of the structure and chemical reactivity of polyhalomethane isomers and polyhalomethane-halogen atom molecular complexes, *J. Chem. Phys.* **117**, 79317941 (2002).
- [14] A. N. Tarnovsky, M. Wall, M. Gustafsson, N. Lascoux, V. Sundström, and E. Åkesson, Ultrafast study of the photodissociation of bromiodomethane in acetonitrile upon 266 nm excitation, *J. Phys. Chem. A* **106**, 5999 (2002).
- [15] J. Vincent, M. Andersson, M. Eklund, A. B. Wöhri, M. Odelius, E. Malmerberg, Q. Kong, M. Wulff, R. Neutze, and J. Davidsson, Solvent dependent structural perturbations of chemical reaction intermediates visualized by time-resolved x-ray diffraction, *J. Chem. Phys.* **130**, 154502 (2009).
- [16] S. Park, J. Choi, H. Ki, K. H. Kim, K. Y. Oang, H. Roh, J. Kim, S. Nozawa, T. Sato, S.-i. Adachi, J. Kim, and H. Ihee, Fate of transient isomer of CH_2I_2 : Mechanism and origin of ionic photoproducts formation unveiled by time-resolved X-ray liquidography, *J. Chem. Phys.* **150**, 224201 (2019).
- [17] E. Jones, T. Oliphant, P. Peterson, *et al.*, SciPy: Open source scientific tools for Python (2001–), [Online; accessed October 15, 2020].
- [18] M. Newville, T. Stensitzki, D. B. Allen, and A. Ingargiola, Lmfit: Non-linear least-square minimization and curve-fitting for python, (2014).

- [19] K. Haldrup, M. Christensen, and M. Meedom Nielsen, Analysis of time-resolved X-ray scattering data from solution-state systems, *Acta Crystallogr. A* **66**, 261 (2010).
- [20] T. B. van Driel, K. S. Kjaer, E. Biasin, K. Haldrup, H. T. Lemke, and M. M. Nielsen, Disentangling detector data in xfel studies of temporally resolved solution state chemistry, *Faraday Discuss.* **177**, 443 (2015).
- [21] K. S. Kjaer, T. B. van Driel, J. Kehres, K. Haldrup, D. Khakhulin, K. Bechgaard, M. Cammarata, M. Wulff, T. J. Sørensen, and M. M. Nielsen, Introducing a standard method for experimental determination of the solvent response in laser pump, X-ray probe time-resolved wide-angle X-ray scattering experiments on systems in solution, *Phys. Chem. Chem. Phys.* **15**, 15003 (2013).
- [22] E. Biasin, T. B. van Driel, G. Levi, M. G. Laursen, A. O. Dohn, A. Moltke, P. Vester, F. B. K. Hansen, K. S. Kjaer, T. Harlang, R. Hartsock, M. Christensen, K. J. Gaffney, N. E. Henriksen, K. B. Møller, K. Haldrup, and M. M. Nielsen, Anisotropy enhanced X-ray scattering from solvated transition metal complexes, *J. Synchrotron Radiat.* **25**, 306 (2018).
- [23] T. K. Kim, J. H. Lee, M. Wulff, Q. Kong, and H. Ihee, Spatiotemporal kinetics in solution studied by time-resolved X-ray liquidography (solution scattering), *ChemPhysChem* **10**, 1958 (2009).
- [24] A. O. Dohn, E. Biasin, K. Haldrup, M. M. Nielsen, N. E. Henriksen, and K. B. M. Iler, On the calculation of X-ray scattering signals from pairwise radial distribution functions, *J. Phys. B-At. Mol. Opt.* **48**, 244010 (2015).
- [25] R. D. B. Fraser, T. P. MacRae, E. Suzuki, and IUCr, An improved method for calculating the contribution of solvent to the X-ray diffraction pattern of biological molecules, *J. Appl. Crystallogr.* **11**, 693 (1978).
- [26] J. Wang, R. M. Wolf, J. W. Caldwell, P. A. Kollman, and D. A. Case, Development and testing of a general amber force field., *J. Comput. Chem.* **25**, 1157 (2004).
- [27] D. van der Spoel, P. J. van Maaren, and C. Caleman, GROMACS molecule & liquid database, *Bioinformatics* **28**, 752 (2012).
- [28] S. Pronk, S. Páll, R. Schulz, P. Larsson, P. Bjelkmar, R. Apostolov, M. R. Shirts, J. C. Smith, P. M. Kasson, D. van der Spoel, B. Hess, and E. Lindahl, GROMACS 4.5: a high-throughput and highly parallel open source molecular simulation toolkit, *Bioinformatics* **29**, 845 (2013).
- [29] W. F. van Gunsteren and H. J. C. Berendsen, A leap-frog algorithm for stochastic dynamics, *Mol. Sim.* **1**, 173 (1988).

- [30] H. J. C. Berendsen, J. P. M. Postma, A. DiNola, and J. R. Haak, Molecular dynamics with coupling to an external bath, *J. Chem. Phys.* **81**, 3684 (1984).
- [31] B. Hess, P-LINCS: A parallel linear constraint solver for molecular simulation, *J. Chem. Theory Comput.* **4**, 116 (2008).
- [32] F. Neese, The orca program system, *Wiley Interdisciplinary Reviews: Computational Molecular Science* **2**, 73 (2012).
- [33] F. Neese, Software update: the orca program system, version 4.0, *Wiley Interdisciplinary Reviews: Computational Molecular Science* , e1327 (2017).
- [34] F. Weigend and R. Ahlrichs, Balanced basis sets of split valence, triple zeta valence and quadruple zeta valence quality for h to rn: Design and assessment of accuracy, *Phys. Chem. Chem. Phys.* **7**, 3297 (2005).
- [35] K. A. Peterson, D. Figgen, M. Dolg, and H. Stoll, Energy-consistent relativistic pseudopotentials and correlation consistent basis sets for the 4d elements ypd, *J. Chem. Phys.* **126**, 124101 (2007), <https://doi.org/10.1063/1.2647019>.
- [36] M. J. Abraham, T. Murtola, R. Schulz, S. Páll, J. C. Smith, B. Hess, and E. Lindahl, GROMACS: High performance molecular simulations through multi-level parallelism from laptops to supercomputers, *SoftwareX* **1**, 19 (2015).
- [37] H. J. C. Berendsen, J. P. M. Postma, W. F. van Gunsteren, A. DiNola, and J. R. Haak, Molecular-dynamics with coupling to an external bath, *J. Chem. Phys.* **81**, 3684 (1984).
- [38] D. Lavalette, C. Tétreau, M. Tourbez, and Y. Blouquit, Microscopic viscosity and rotational diffusion of proteins in a macromolecular environment, *Biophys. J.* **76**, 2744 (1999).
- [39] M. Horng, J. Gardecki, and M. Maroncelli, Rotational dynamics of coumarin 153: time-dependent friction, dielectric friction, and other nonhydrodynamic effects, *J. Phys. Chem. A* **101**, 1030 (1997).
- [40] T. Gomti Devi and K. Kumar, Raman bandshape analysis of o-chlorobenzaldehyde: Microviscosity-dependent study, *Journal of Raman Spectroscopy* **35**, 835 (2004).
- [41] A. Gierer and K. Wirtz, Molekulare theorie der mikroreibung, *Z. Naturforsch., A: Phys. Sci.* **8**, 532 (1953).
- [42] N. Michaud-Agrawal, E. J. Denning, T. B. Woolf, and O. Beckstein, Mdanalysis: A toolkit for the analysis of molecular dynamics simulations, *Journal of Computational Chemistry* **32**, 2319 (2011).
- [43] Richard J. Gowers, Max Linke, Jonathan Barnoud, Tyler J. E. Reddy, Manuel N. Melo, Sean L. Seyler, Jan Domański, David L. Dotson, Sébastien Buchoux, Ian M. Kenney, and Oliver Beckstein, MDAnal-

ysis: A Python Package for the Rapid Analysis of Molecular Dynamics Simulations, in *Proceedings of the 15th Python in Science Conference*, edited by Sebastian Benthall and Scott Rostrup (2016) pp. 98 – 105.

- [44] M. D. Hanwell, D. E. Curtis, D. C. Lonie, T. Vandermeersch, E. Zurek, and G. R. Hutchison, Avogadro: an advanced semantic chemical editor, visualization, and analysis platform, *J. Cheminformatics* **4**, 10.1186/1758-2946-4-17 (2012).